

# Nonideal MHD Effects and Magnetic Braking Catastrophe in Protostellar Disk Formation

Zhi-Yun Li<sup>1,2</sup>, Ruben Krasnopolsky<sup>2,3</sup>, Hsien Shang<sup>2,3</sup>

## ABSTRACT

Dense, star-forming, cores of molecular clouds are observed to be significantly magnetized. A realistic magnetic field of moderate strength has been shown to suppress, through catastrophic magnetic braking, the formation of a rotationally supported disk during the protostellar accretion phase of low-mass star formation in the ideal MHD limit. We address, through 2D (axisymmetric) simulations, the question of whether realistic levels of nonideal effects, computed with a simplified chemical network including dust grains, can weaken the magnetic braking enough to enable a rotationally supported disk to form. We find that ambipolar diffusion, the dominant nonideal MHD effect over most of the density range relevant to disk formation, does not enable disk formation, at least in 2D. The reason is that ambipolar diffusion allows the magnetic flux that would be dragged into the central stellar object in the ideal MHD limit to pile up instead in a small circumstellar region, where the magnetic field strength (and thus the braking efficiency) is greatly enhanced. We also find that, on the scale of tens of AU or more, a realistic level of Ohmic dissipation does not weaken the magnetic braking enough for a rotationally supported disk to form, either by itself or in combination with ambipolar diffusion. The Hall effect, the least explored of these three nonideal MHD effects, can spin up the material close to the central object to a significant, supersonic rotation speed, even when the core is initially non-rotating, although the spun-up material remains too sub-Keplerian to form a rotationally supported disk. The problem of catastrophic magnetic braking that prevents disk formation in dense cores magnetized to realistic levels remains unresolved. Possible resolutions of this problem are discussed.

*Subject headings:* accretion, accretion disks — magnetic fields — ISM: clouds — stars: formation — magnetohydrodynamics (MHD)

---

<sup>1</sup>University of Virginia, Astronomy Department, Charlottesville, USA

<sup>2</sup>Academia Sinica, Theoretical Institute for Advanced Research in Astrophysics, Taipei, Taiwan

<sup>3</sup>Academia Sinica, Institute of Astronomy and Astrophysics, Taipei, Taiwan

## 1. Introduction

The formation and early evolution of disks is a long-standing fundamental problem in star formation. Early work in the field had concentrated on the simpler problem of disk formation from the collapse of a rotating dense core in the absence of a magnetic field, as reviewed in Bodenheimer (1995) and Boss (1998). Dense star-forming cores are observed to be significantly magnetized, however. There is increasing theoretical evidence that disk formation is greatly modified, perhaps even suppressed, by a dynamically important magnetic field.

The most comprehensive measurements of the magnetic field strength in dense cores of low-mass star formation come from Troland & Crutcher (2008). They carried out an OH Zeeman survey of a sample of nearby dark cloud cores, probing densities of order  $10^3$ – $10^4 \text{ cm}^{-3}$ . The inferred mean value for the dimensionless mass-to-flux ratio, relative to the critical value  $(2\pi G^{1/2})^{-1}$  (Nakano & Nakamura 1978, Shu & Li 1997), is  $\lambda_{los} \approx 4.8 \pm 0.4$ . It was obtained from the measured line-of-sight component of the magnetic field  $B_{los}$  without any geometric correction. Correcting for geometric effects statistically would lower the mass-to-flux ratio by a factor of 2–3 (Shu et al. 1999), bringing the mean value of the intrinsic mass-to-flux ratio to a few, i.e.,  $\lambda \sim 2$ –3. Such values of  $\lambda$  are naturally produced in the scenario of ambipolar diffusion-regulated dense core formation in strongly magnetized (magnetically subcritical) clouds, with or without the assistance of supersonic turbulence (e.g., Lizano & Shu 1989; Basu & Mouschovias 1994; Nakamura & Li 2005; Kudoh & Basu 2011). It may also be consistent with the scenario of dense core formation from turbulence compression in more weakly magnetized background clouds, since the core is expected to be more strongly magnetized relative to its mass (i.e., lower  $\lambda$ ) than the cloud as a whole (Tilley & Pudritz 2005; Dib et al. 2007). Well ordered magnetic fields are also inferred from polarization maps of dust continuum emission, both on the core scale (Ward-Thompson et al. 2000) and smaller (e.g., Girart et al. 2006). We therefore expect the dense cores to be rather strongly magnetized based on both observational data and core formation theories.

A moderately strong magnetic field can suppress disk formation in the ideal MHD limit. This was first demonstrated in Allen et al. (2003), who carried out 2D (axisymmetric) simulations of the collapse of rotating cores magnetized to a level of  $\lambda \leq 10$ . The basic reason for disk suppression is that, in the ideal MHD limit, flux freezing allows the infalling material to drag a finite amount of magnetic flux into the central object, creating a split magnetic monopole whose (poloidal) field strength increases rapidly with decreasing radius (as  $r^{-2}$ , Galli et al. 2006; see their Fig. 1). The increased field strength close to the central object, coupled with a long magnetic lever arm from severe equatorial pinching of (poloidal) field lines, is responsible for the catastrophic magnetic braking that suppresses the formation of a

rotationally supported disk. This magnetic braking catastrophe was confirmed numerically by Mellon & Li (2008) and Hennebelle & Fromang (2008) using, respectively, 2D and 3D simulations (see also Price & Bate 2007), at least when the magnetic and rotation axes are aligned (see, however, Machida et al. 2010 and discussion in §6).

When the magnetic and rotation axes are misaligned, Hennebelle & Ciardi (2009) found in their AMR MHD simulations that magnetic braking efficiency is reduced relative to the aligned case. A potential concern is that the misalignment increases the flow complexity, which may enhance the numerical magnetic diffusion that is considerable on small scales (see a nice discussion in §5.3 of Hennebelle et al. 2011). A more obvious possibility for avoiding the magnetic braking catastrophe is to relax the ideal MHD approximation. Since dense cores are known to be lightly ionized (Bergin & Tafalla 2007), non-ideal MHD effects (including ambipolar diffusion, Hall effect and Ohmic dissipation, e.g., Nakano et al. 2002) are to be expected. The first non-ideal MHD effect considered in this context was Ohmic dissipation. Shu et al. (2006) suggested that in order for Ohmic dissipation to weaken the field strength over a large enough region so that a large-scale rotationally supported disk of tens of AUs or more can potentially form, the resistivity must be at least one order of magnitude above the classical (microscopic) value. This suggestion was confirmed by Krasnopolsky et al. (2010), who found that large, 100 AU scale disks can indeed form, as long as the resistivity is enhanced by a large enough factor, to a value of order  $10^{19} \text{ cm}^2 \text{ s}^{-1}$  or more. Machida et al. (2010) carried out core collapse calculations including a distribution of resistivity with density and temperature (from a fit to the resistivities computed in Nakano et al. 2002) and found that, even with just the classical resistivity, a small rotationally supported disk can form at the beginning of the protostellar accretion phase (see also Dapp & Basu 2010) and grow to larger, 100-AU scales at later times. Part of the apparent discrepancy between Machida et al. (2010) and Krasnopolsky et al. (2010) may be due to different simulation setup. Another difference may be in the level of numerical magnetic diffusivity (see discussion in §6). Further investigation is needed to clarify the situation in the limiting case that includes only Ohmic dissipation.

Ohmic dissipation is important at high densities (above  $\sim 10^{11} \text{ cm}^{-3}$ , Nakano et al. 2002; see also Kunz & Mouschovias 2010). Before reaching such densities, dense core material must evolve through lower densities, where the Hall effect and especially ambipolar diffusion dominate over Ohmic dissipation. The effect of ambipolar diffusion on disk formation was investigated semi-analytically by Krasnopolsky & Königl (2002), and numerically by Mellon & Li (2009; see also Duffin & Pudritz 2009 and Hosking & Whitworth 2004). Compared to the ideal MHD case, a new ingredient is the ambipolar diffusion-induced accretion shock, driven by the magnetic flux left behind by the material that has gone into the central object (Li & McKee 1996; Ciolek & Königl 1998; Contopoulos et al. 1998;

Tassis & Mouschovias 2007). Krasnopolsky & Königl (2002) demonstrated using a 1D semi-analytic model that the strong magnetic field piled up inside the ambipolar diffusion (AD) shock can in principle brake the post-shock material efficiently. Mellon & Li (2009) showed through 2D (axisymmetric) simulations that this is indeed the case. They started their calculations from a self-similar rotating, magnetized isothermal toroid (Allen et al. 2003). A power-law dependence on the neutral density is assumed for the ion density, so that the subsequent collapse remains self-similar, even in the presence of ambipolar diffusion. The self-similarity provides a powerful check on the validity of the numerically obtained collapse solutions. It imposes, however, strong restrictions on both the initial core properties and charge densities.

One objective of the present paper is to investigate the role of ambipolar diffusion in disk formation without the restrictive simplifications made in Mellon & Li (2009). We do this by following both the pre-stellar evolution of the rotating, magnetized dense core and the protostellar mass accretion phase after a central stellar object has formed and by computing the charge densities self-consistently using a simplified chemical network that includes dust grains (Nishi et al. 1991; Nakano et al. 2002); they can affect the magnetic diffusivities greatly (e.g., Wardle & Ng 1999). Another objective is to extend Mellon & Li’s (2009) calculations by including both Ohmic dissipation and Hall effect in addition to ambipolar diffusion. The Hall effect was explored previously in the context of disk-driven outflows (Wardle & Königl 1993; see also Königl et al. 2010) and accretion disk dynamics (Sano & Stone 2002); it is only starting to be explored in the context of core collapse and disk formation (Krasnopolsky et al. 2011; C. Braiding 2011).

We find that, on scales greater than  $10^{14}$  cm (or 6.7 AU) that we are able to resolve in our non-ideal MHD calculations, no rotationally supported disks form in dense cores with a moderately strong magnetic field (with  $\lambda \sim$  several), largely because of the excessive braking due to the magnetic field trapped interior to the AD shock. On these scales, Ohmic dissipation affects the flow dynamics relatively little. The Hall effect, on the other hand, can torque up the spun-down post AD-shock material to significant, supersonic, rotation speeds. The rotation speeds remain well below Keplerian and rotationally supported disks are not formed. Our non-ideal MHD calculations re-enforce the idea that disk formation is difficult in the presence of a moderately strong magnetic field, at least in 2D (assuming axisymmetry). We discuss possible ways to get around this difficulty in the discussion section (§6).

The rest of the paper is organized as follows. In §2, we describe the problem setup, including the initial and boundary conditions, the nonideal MHD code used in this work, and the computation of charge densities including dust grains. Disk suppression by a moderately

strong magnetic field under a range of realistic conditions is demonstrated in §3. We discuss potential disk formation in the case of weaker magnetic fields in §4 and the spin up of an initially non-rotating collapsing envelope by the Hall effect in §5. Our main results are summarized §7.

## 2. Problem Setup

### 2.1. Initial and Boundary Conditions

Low-mass pre-stellar cores in nearby star-forming regions are observed to have relatively simple dynamical structures (Bergin & Tafalla 2007). We idealize such cores as initially uniform spheres of  $R = 10^{17}$  cm in mass and  $1 M_{\odot}$  in mass (see Hennebelle & Fromang 2008 for a similar setup). The initial core mass density is thus  $\rho_0 = 4.77 \times 10^{-19} \text{ g cm}^{-3}$ , corresponding to a volume density for molecular hydrogen  $n_{H_2} = 10^5 \text{ cm}^{-3}$  (assuming 10 hydrogen nuclei for each He), and a free fall time  $t_{ff} = 3 \times 10^{12}$  s. A simple isothermal equation of state is adopted below a critical density  $\rho = 10^{-13} \text{ g cm}^{-3}$  (with a sound speed  $a = 0.2 \text{ km s}^{-1}$ ) and  $P \propto \rho^{7/5}$  at densities above (e.g., Masunaga & Inutsuka 2000). The ratio of thermal to gravitational binding energy is  $\alpha = 2.5Ra^2/(GM) = 0.75$ . On this uniform sphere, we impose a uniform magnetic field  $B_0$  at the beginning of the simulation. We choose a fiducial value for  $B_0$  of  $10^{-5}$  in the Lorentz-Heaviside units that are convenient for the Zeus family of codes. It corresponds to  $B_0 = \sqrt{4\pi} \times 10^{-5} \text{ G} = 35.4 \mu\text{G}$  in Gaussian CGS units. The ratio of magnetic to gravitational binding energy is  $\gamma = 0.13$ . Another way to characterize the strength of the magnetic field is through the dimensionless mass-to-flux ratio  $\lambda$ , in units of the critical value  $(2\pi G^{1/2})^{-1}$ . For the core as a whole, the mass-to-flux ratio is  $\lambda = 2.92$ . On the central flux tube that passes through the origin, the mass-to-flux ratio is  $\lambda_c = 4.38$ , higher than the global value by 50%. These fiducial values of mass-to-flux ratios are somewhat larger than the values of  $\lambda \sim 2\text{--}3$  obtained in models of ambipolar-diffusion driven core formation out of magnetically subcritical background clouds, with (Nakamura & Li 2005; Kudoh & Basu 2011) or without (Lizano & Shu 1989; Basu & Mouschovias 1994) turbulent compression. They are consistent with the mean value of  $\lambda$  inferred by Troland & Crutcher (2008) after correcting for geometric effects (see §1).

One may argue that the adopted fiducial field strength of  $B_0 = 35.4 \mu\text{G}$  at a number density  $n_{H_2} = 10^5 \text{ cm}^{-3}$  is too high, because such a field strength is rarely measured in nearby regions of low-mass star formation (such as the Taurus clouds) directly using OH. However, the OH emission is dominated by relatively low density envelopes of dense cores (Troland & Crutcher 2008). If the core material was condensed out of a more diffuse gas, its field strength would be lower before condensation. For example, at densities of order  $n_{H_2} \sim$

$10^{3.5} \text{ cm}^{-3}$  (probed by typical OH observations; Crutcher et al. 2010), the pre-condensation field strength of our model core would be only  $\sim 3.5 \mu\text{G}$  (if the condensation occurs more or less isotropically under flux-freezing condition, as it should be since the core is substantially magnetically supercritical). It is lower than the medium value of  $\sim 6 \mu\text{G}$  inferred for the *atomic* cold neutral medium (Heiles & Troland 2005). If anything, our adopted fiducial field strength may be on the low side. Nevertheless, we will consider some smaller values for  $B_0$  as well, in view of the possibility that there may be a broad distribution of field strengths at a given density (Crutcher et al. 2010) and the fact that the majority of stars are formed in clusters where the magnetic field is less well observed.

One may also be concerned that our adopted initial density distribution is uniform, whereas the observed pre-stellar cores are centrally condensed (Bergin & Tafalla 2007). However, the density distribution changes with time, evolving through a series of centrally condensed configurations with different degrees of central-to-edge contrast, as seen in Fig. 1 in the absence of magnetic field and rotation. For example, the central density  $n_{H_2} \sim 10^6 \text{ cm}^{-3}$  at time  $2.5 \times 10^{12} \text{ s}$  is close to that inferred for the well studied pre-stellar core L1544 (Ward-Thompson et al. 1999), although the maximum infall speed at this time is somewhat higher than the observationally inferred value, which is roughly  $10^4 \text{ cm s}^{-1}$  (Tafalla et al. 1998). The infall speed is reduced, however, by both rotation and especially magnetic fields that are included in the majority of our calculations. Indeed, the infall is approximately half-sonic for our reference model (see Table 1) when the central density  $n_{H_2} \sim 10^6 \text{ cm}^{-3}$ , in agreement with observations.

An alternative approach would be to start with a centrally condensed static configuration that mimics the observed pre-stellar density profile, with a uniform magnetic field imposed at the beginning (e.g., Machida et al. 2007). Implicit in this approach is the assumption that there is strong evolution in the density profile of the core but no corresponding evolution in its magnetic field distribution. For our purpose of studying the efficiency of magnetic braking, it has the drawback that the central flux tubes are loaded with much more mass than those in the outer part. It would lead to a weaker magnetic braking in the early phase of protostellar collapse that, in our view, is hard to justify physically.

The rotating profile of dense cores is not well constrained by observations. For simplicity, we adopt for our initially uniform core a solid body rotation, with a fiducial angular speed  $\Omega = 10^{-13} \text{ s}^{-1}$ . It corresponds to a ratio of rotational to gravitational binding energy  $\beta = 0.025$ , which is typical of the values inferred for  $\text{NH}_3$  cores based on the velocity gradient observed across the cores (Goodman et al. 1993); the inferred  $\beta$  has a considerable range, which motivates us to consider other values of  $\beta$  as well.

As in Mellon & Li (2008, 2009), we adopt a spherical polar coordinate system  $(r, \theta, \phi)$

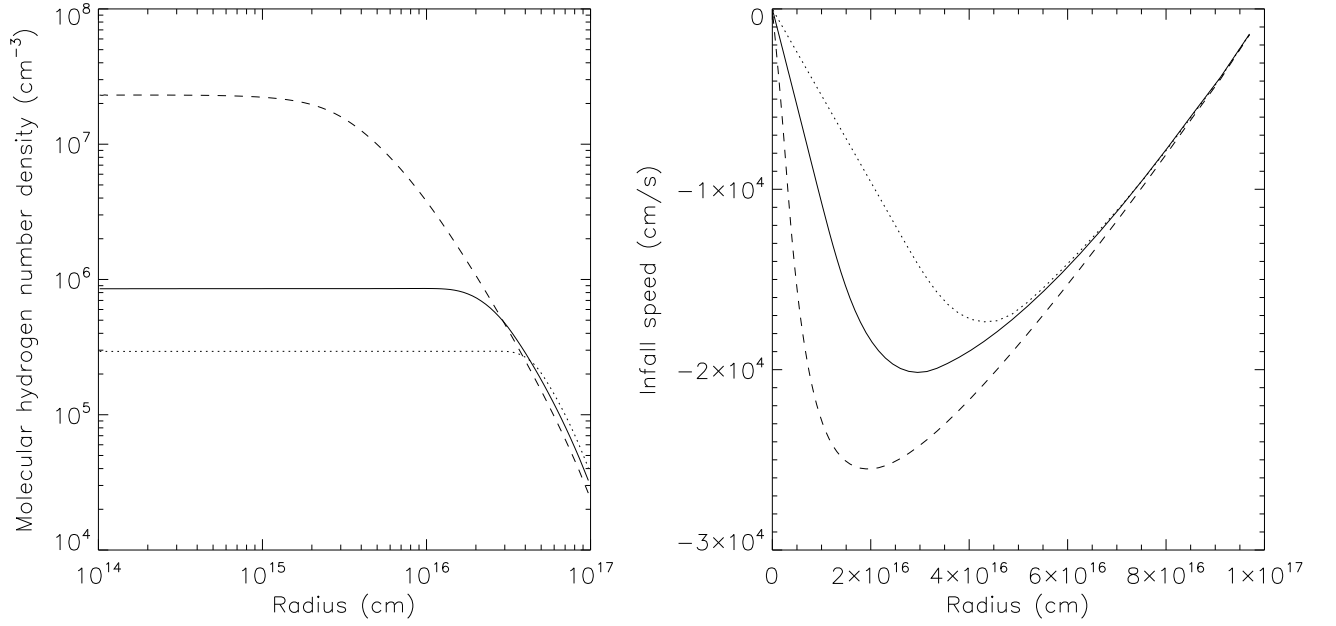


Fig. 1.— Distributions of the density (left panel) and infall velocity (right) at three times  $2 \times 10^{12}$  (dotted line),  $2.5 \times 10^{12}$  (solid) and  $3 \times 10^{12}$  s (dashed) for the collapse of a non-rotating, non-magnetized dense core.



for our axisymmetric simulation. The inner boundary is set at  $10^{14}$  cm (or 6.7 AU) and the outer boundary at  $10^{17}$  cm. Even though our inner radius is relatively large compared with other collapse studies, such as Machida et al. (2010) who set the sink particle size to 1 AU, our smallest cell size is only 0.2 AU, which ensures that the flow dynamics near the inner boundary is well resolved. The high resolution is particularly important for minimizing the numerical magnetic diffusion that may affect the trapping of magnetic flux at small radii, which lies at the heart of efficient magnetic braking and disk suppression. The standard outflow boundary conditions are enforced at both the inner and outer boundaries. Matter that crosses the inner boundary is collected at the origin. The central point mass interacts with the matter in the computation domain through gravity. We use a computational grid of  $120 \times 90$  that is non-uniform in the  $r$ -direction, with a spacing  $\Delta r = 0.2$  AU next to the inner boundary. The spacing increases outward by a constant factor  $\sim 1.0647$  from one cell to the next. The grid is uniform in the  $\theta$ -direction.

## 2.2. Induction Equation and Non-Ideal MHD Code

At the heart of our non-ideal MHD core collapse problem lies the induction equation

$$\frac{\partial \mathbf{B}}{\partial t} = \nabla \times (\mathbf{v} \times \mathbf{B}) - \nabla \times [\eta_O (\nabla \times \mathbf{B})] - \nabla \times \left\{ \eta_H [(\nabla \times \mathbf{B}) \times \frac{\mathbf{B}}{B}] \right\} - \nabla \times \left\{ \eta_A \frac{\mathbf{B}}{B} \times [(\nabla \times \mathbf{B}) \times \frac{\mathbf{B}}{B}] \right\} \quad (1)$$

where the Ohmic, Hall and ambipolar diffusivities are related to the electric conductivity parallel to the field line  $\sigma_{\parallel}$ , Pedersen and Hall conductivities  $\sigma_P$  and  $\sigma_H$  through (Nakano et al. 2002)

$$\eta_O = \frac{c^2}{4\pi\sigma_{\parallel}}; \quad \eta_H = \frac{c^2}{4\pi} \frac{\sigma_H}{\sigma_P^2 + \sigma_H^2}; \quad \eta_A = \frac{c^2}{4\pi} \left( \frac{\sigma_P}{\sigma_P^2 + \sigma_H^2} - \frac{1}{\sigma_{\parallel}} \right). \quad (2)$$

These diffusivities will be discussed further in the next subsection. Here, we describe briefly our numerical treatment of the three non-ideal MHD terms.

Our code, dubbed “ZeusTW,” was derived from the ideal MHD code Zeus3D (Clarke et al. 1994). It treats the Ohmic term in the induction equation (1) using an algorithm based on Fleming et al. (2000; see also Krasnopolsky et al. 2010). Ambipolar diffusion was treated using the explicit method described in Mac Low et al. (1995), as in Mellon & Li (2009). The magnetic field is evolved using a velocity that is the sum of the bulk neutral velocity  $\mathbf{v}$  and a “drift” velocity defined as

$$\Delta \mathbf{v}_{AD} = \frac{\eta_A}{B^2} (\nabla \times \mathbf{B}) \times \mathbf{B}. \quad (3)$$

In the widely discussed limit where ambipolar diffusion is the dominant non-ideal effect and ions are well tied to the magnetic field, the velocity  $\Delta \mathbf{v}_{AD}$  can be interpreted as the ion-



neutral drift velocity. In the more general case that we are studying, this is not necessarily the case. Nevertheless, we will define an “effective ion velocity”

$$\mathbf{v}_{i,\text{eff}} \equiv \Delta \mathbf{v}_{AD} + \mathbf{v}, \quad (4)$$

to make contact with previous work. It provides a useful measure of the effect of ambipolar diffusion even in the presence of other non-ideal MHD effects. Lastly, our treatment of the Hall term was based on Sano & Stone (2002) and Huba (2003, see Krasnopolsky et al. 2011 for detail). The time steps for evolving the ambipolar diffusion and Hall terms in the induction equation are particularly stringent near the polar axes, where the magnetic field is strong but the density is often low, due to either gravitational collapse along the field lines or outflow. In some cases, a floor is imposed on the time step, by decreasing the ambipolar or Hall diffusivity in a small volume or increasing the density in an evacuated region to limit the Alfvén speed. We have verified that the floor has little effect on the flow dynamics.

### 2.3. Charge Densities and Magnetic Diffusivities

The magnetic diffusivities depend on the densities of charged particles, including molecular and atomic ions, electrons, and charged dust grains. We will follow Nakano and collaborators in computing the charge densities (e.g., Nakano et al. 2002; Nishi et al. 1991), using a simplified chemical network and simple prescriptions for grain size distribution. The network includes neutral species  $\text{H}_2$ ,  $\text{He}$ ,  $\text{CO}$ ,  $\text{O}$ ,  $\text{O}_2$  and other heavy metals (denoted collectively by “M”) and charged species  $e^-$ ,  $\text{H}^+$ ,  $\text{He}^+$ ,  $\text{C}^+$ ,  $\text{M}^+$ ,  $\text{H}_3^+$ , and other molecular ions (denoted collectively by “ $m^+$ ”), as well as neutral and positively and negatively charged dust grains (see Nishi et al. 1991 for detail). The grain size distribution in dense cores of molecular clouds is relatively unconstrained observationally. For illustration, we will consider the standard MRN distribution ( $dn/da \propto a^{-3.5}$  with the grain size  $a$  between  $5 \text{ nm} < a < 250 \text{ nm}$  (Mathis et al. 1977) and a grain mass that is 1% of the total. It is likely, however, for the grains to grow substantially in dense cores of molecular clouds; the MRN distribution, which is more appropriate for diffuse clouds, may be regarded as the starting point for grain growth in dense cores. Direct evidence for grain growth comes from the Spitzer detection of the so-called “coreshine” (Pagani et al. 2010), which indicates that at least some grains have grown to micron-size. To illustrate the effects of grain growth, we will also consider an opposite limit where the grains have a single, large, size  $a = 1 \mu\text{m}$  (denoted LG distribution). The MRN and LG distributions should bracket the real situation where some grain growth is expected.

Fig. 2 plots the fractional abundances (relative to the number density of hydrogen nuclei  $n_H$ ) of the charged atomic and molecular species and dust grains as a function of

$n_H$  (related to mass density through  $\rho = 2.34 \times 10^{-24} n_H$ ), with the cosmic rate ionization rate  $\zeta$  normalized to the standard value  $10^{-17} \text{ s}^{-1}$ ; the normalized rate is denoted by  $\zeta_{17} = \zeta / (10^{-17} \text{ s}^{-1})$ . In the (simpler) large grain (LG) case, the dominant charges are metal ions ( $M^+$ ) and electrons ( $e^-$ ) over the whole density range of interest to us. In the MRN case, the charge densities are lower compared to the LG case, because of a large amount of small grains, which provide a large total surface area for ions and electrons to recombine on. The metal ions and electrons remain the most abundant charges at low densities (below  $\sim 10^6 \text{ cm}^{-3}$ ). At higher densities, negatively and positively charged (small) grains become more dominant. The MRN case was computed with 10 size bins equally spaced logarithmically, following Nishi et al. (1991). When 20 bins are used, the charge densities change by less than 3% over the density range that spans more than 10 orders of magnitude.

To obtain the magnetic diffusivities in the induction equation, we need not only charge densities, but also magnetic field strength. The field strength will be computed self-consistently in our MHD simulations. The rough magnitude of the diffusivities can be illustrated using e.g. the field strength-density relation

$$B = 1.43 \times 10^{-7} n_H^{1/2} \quad (5)$$

assumed in Nakano et al. (2002), relevant for a magnetically supported sheet in hydrostatic equilibrium along the field lines. The computed diffusivities are shown in Fig. 3. As expected, the ambipolar diffusivity dominates at relatively low densities for both MRN and LG cases. For the MRN case, which has a large amount of small grains, the Hall diffusivity becomes comparable to the ambipolar diffusivity over a wide range of density ( $\sim 10^8 - 10^{12} \text{ cm}^{-3}$ ). It has a negative value, dominated by the contribution from negatively charged grains, although the contribution from positively charged grains approaches (from below) that from the negative grains at densities greater than  $\sim 10^{10} \text{ cm}^{-3}$ . At densities greater than  $\sim 10^{12} \text{ cm}^{-3}$  (which is generally not reached in our computational domain), Ohmic diffusivity dominates. The large Ohmic diffusivity  $\eta_O$  is the reason for the ambipolar diffusivity  $\eta_A$  to become negative above a density  $\sim 10^{12} \text{ cm}^{-3}$ , since it contributes negatively to  $\eta_A$  (see eq. [2]). In the opposite extreme of large grain case (LG), where all small grains are removed, the Hall diffusivity is positive, dominated by the contribution from metal ions. It exceeds the ambipolar diffusivity above a density  $n_H \sim 10^{12} \text{ cm}^{-3}$ . In this case, the level of ionization is high enough that the Ohmic diffusivity remains unimportant throughout the plotted density range (up to  $\sim 10^{15} \text{ cm}^{-3}$ ). Overall, the elimination of small grains in the LG case makes the magnetic field better coupled to the bulk neutral material compared to the MRN case, as expected.

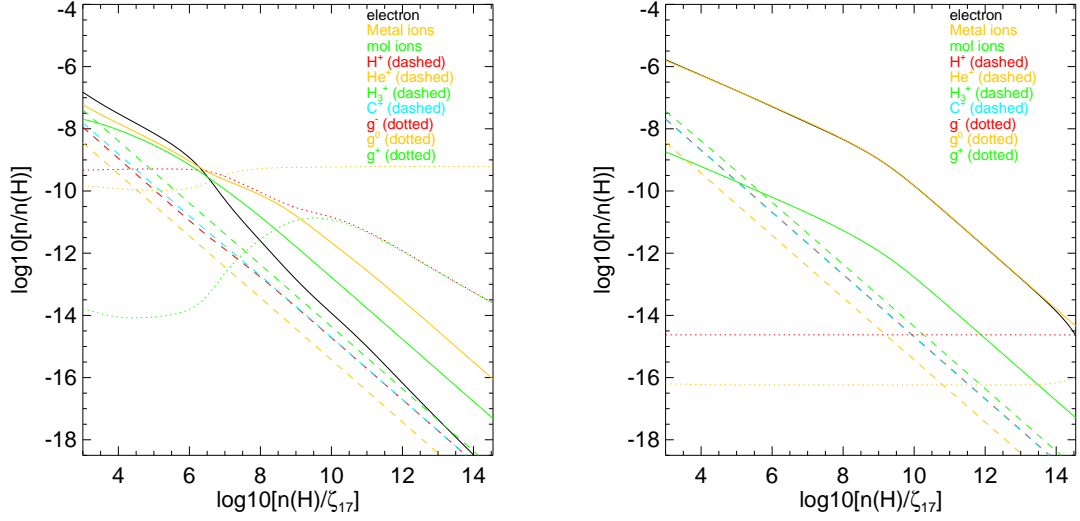


Fig. 2.— The number densities of charges for the standard MRN grain size distribution (left panel) and large,  $1 \mu\text{m}$  grains (right).

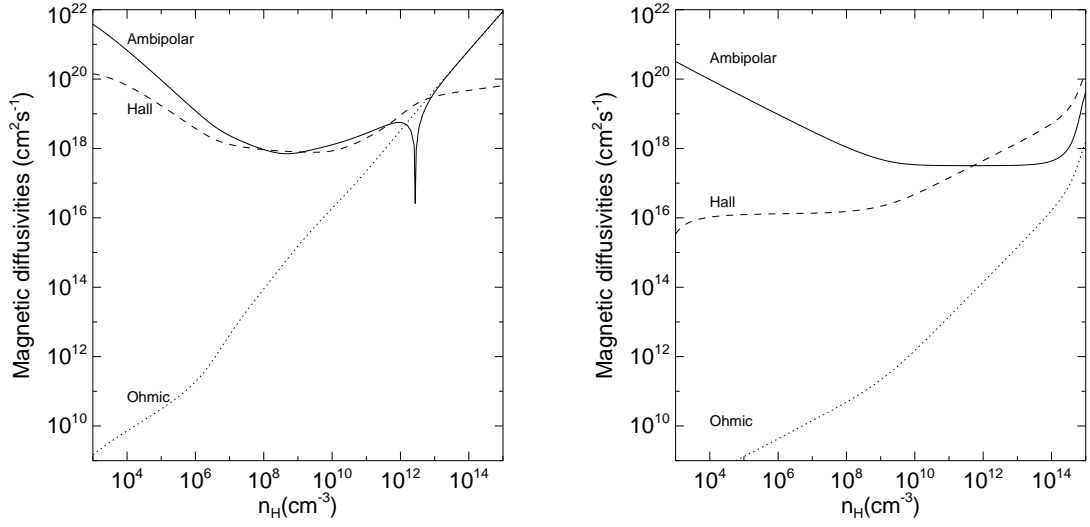


Fig. 3.— The absolute values of the computed magnetic diffusivities for the MRN (left panel) and large grain (right panel) cases, for the illustrative magnetic field-density relation given in eq. (5). For the MRN case, the Hall diffusivity  $\eta_H$  is negative everywhere and the ambipolar diffusivity  $\eta_A$  changes from positive to negative as the density  $n_H$  increases above  $\sim 10^{12} \text{ cm}^{-3}$ .

### 3. Disk Suppression by a Moderately Strong Magnetic Field

In this section, we will consider a magnetic field of moderate strength  $B_0 = 35.4 \mu\text{G}$ , corresponding to a dimensionless mass-to-flux ratio of  $\lambda = 2.92$  for the dense ( $n_{H_2} = 10^5 \text{ cm}^{-3}$ ) core as a whole and 4.38 for the central flux tube. As we argued in §1, this field strength is likely on the conservative side. Since the ambipolar diffusivity dominates over the Ohmic and Hall diffusivities in most of the density range encountered in our calculations (see Fig. 3), we will first concentrate on its effect on core collapse and disk formation in §3.1 and §3.2. Similar AD-only calculations were performed by Mellon & Li (2009), except that we now include the prestellar phase of core evolution leading up to the formation of a central object (in addition to the protostellar phase that they studied) and a more detailed calculation of the charge densities, including charged grains. The additional effects of the Ohmic and Hall diffusivities are considered in §3.3 and §3.4, respectively.

#### 3.1. Reference Model with Ambipolar Diffusion Only

For the reference model, we adopt the fiducial values for the initial field strength  $B_0 = 35.4 \mu\text{G}$ , cosmic ray ionization rate  $\zeta = 10^{-17} \text{ s}^{-1}$ , and initial core rotation rate  $\Omega_0 = 10^{-13} \text{ s}^{-1}$ , as well as an MRN grain size distribution. Since grain growth in dense cores tends to make the magnetic field better coupled to the neutral matter (see Fig. 3) and magnetic braking more efficient, our adoption of the MRN distribution is also on the conservative side. The parameters for this (Model REF) and other models are listed in Table 1. The results are shown in Figs. 4, 5 and 6.

Fig. 4 displays the density distribution and velocity field on the meridian and equatorial planes for the inner part ( $10^3$ -AU scale) of the computation domain, at a representative time  $t = 6 \times 10^{12} \text{ s}$  (or twice the initial free-fall time), when  $0.57 M_\odot$  (or 57% of the initial core mass) has fallen to the center. From the left panel, it is clear that the density distribution on the meridian plane is highly flattened, especially at high densities. The dense, flattened, equatorial structure is *not* a rotationally supported disk, however. Direct evidence against such a disk comes from the right panel, which shows a transition from an outer region of rapid rotating-infall to an inner region that is neither collapsing nor rotating rapidly. The transition is shown more quantitatively in the left panel of Fig. 5, where the infall and rotation speeds on the equator are plotted. The equatorial infall is initially slowed down near a relatively large radius  $r = 5 \times 10^{16} \text{ cm}$ . It corresponds to the edge of the magnetic bubble inflated by magnetic braking (not shown in Fig. 4), where a magnetic barrier forces the collapsing material over a large solid angle into a narrow equatorial channel (see Fig. 2 of Mellon & Li 2008 and associated discussion). Upon passing through the barrier, the material

Table 1. Model Parameters

Model <sup>a</sup>	Grain	$B_0$ ( $\mu\text{G}$ )	$\zeta(10^{-17} \text{ s}^{-1})$	$\Omega_0(10^{-13} \text{ s}^{-1})$	RSD? <sup>b</sup>
REF	MRN	35.4	1	1	no
LG	LG	35.4	1	1	no
LoCR	MRN	35.4	0.1	1	no
HiCR	MRN	35.4	3	1	no
LoROT	MRN	35.4	1	0.5	no
HiROT	MRN	35.4	1	2	no
REF <sub>AO</sub>	MRN	35.4	1	1	no
REF <sub>O</sub>	MRN	35.4	1	1	no
REF <sub>AHO</sub> <sup>-</sup>	MRN	35.4	1	1	no
REF <sub>AHO</sub> <sup>+</sup>	MRN	35.4	1	1	no
WREF	MRN	10.6	1	1	no
WLG	LG	10.6	1	1	no
WHiCR	MRN	10.6	3	1	no
WLoROT	MRN	10.6	1	0.5	no
WLoCR	MRN	10.6	0.5	1	yes?
WHiROT	MRN	10.6	1	2	yes?
VWREF	MRN	3.54	1	1	yes?
NoROT <sub>AHO</sub> <sup>-</sup>	MRN	35.4	1	0	no
NoROT <sub>AHO</sub> <sup>+</sup>	MRN	35.4	1	0	no

Note. — a) The subscript “A,” “H” and “O” denote, respectively, “ambipolar diffusion,” “Hall effect,” and “Ohmic dissipation” included in a model; models without a subscript include only ambipolar diffusion. The superscript “-” (“+”) denotes an initial magnetic field anti-parallel (parallel) to the rotation axis. b) RSD stands for “rotationally supported disk.” In Model WREF, a small RSD is formed temporarily at early times; it is subsequently suppressed by magnetic braking. For Models WLoCR, WHiROT and VWREF, an RSD forms early but whether it would survive to later times remains unclear because of numerical difficulty.

resumes rapid radial infall, spinning up as it collapses, until a second barrier is encountered at  $r \sim 8 \times 10^{15}$  cm. This second barrier is induced by ambipolar diffusion, which enables the magnetic field lines to decouple from matter and pile up outside the central object as the matter accretes onto the protostar (see discussion in §1). The piled-up magnetic field drives a C-shock, which slows down the accretion flow to a subsonic speed. The slowdown of infall leads to a high density in the postshock region, which is clearly visible in the density maps (Fig. 4). Upon passing through the shock, the equatorial material re-accelerates towards the central object, reaching a highly supersonic infall speed at small radii. The supersonic infall clearly indicates that a rotationally supported disk (RSD hereafter for short) is not present.

The lack of an RSD is even more obvious from the rotation speed on the equator plotted in Fig. 5. As the infalling material enters the AD shock, its rotation speed drops quickly. Over most of the postshock region, the rotation speed is nearly zero, indicating an efficient braking of the material that accretes onto the central object through the equatorial region.

Why is it that the rotation of the infalling material is braked almost completely? The answer lies in the strong magnetic field trapped interior to the AD shock (Li & McKee 1996; Contopoulos et al. 1998; Krasnopolsky & Königl 2002). The field trapping is already evident in the left panel of Fig. 4, which shows a pileup of poloidal magnetic field lines at small radii. It is shown more quantitatively in the right panel of Fig. 5, where the distribution of the magnetic pressure ( $B^2/[8\pi]$ ) with radius is plotted along the equator. Note the rapid increase in magnetic pressure (and thus field strength) across the AD shock (near  $r_s \sim 8 \times 10^{15}$  cm). There is a corresponding drop in the ram pressure ( $\rho v_r^2$ ), indicating that the strong post-shock magnetic field is trapped by the ram pressure of the pre-shock collapsing flow (Li & McKee 1996). The further rise in the ram pressure at smaller radii is due to the gravity of the central object, which re-accelerates the equatorial material (that was temporarily slowed down to a subsonic speed behind the AD shock) to a highly supersonic speed. The “effective ion speed” in the post-shock region is much lower than that of the bulk neutral material (see the right panel of Fig. 4). The relatively large drift velocity  $\Delta \mathbf{v}_{AD}$ , driven by a large outward magnetic force, is what enables the magnetic flux to accumulate in the postshock region in the first place: as more and more matter accretes onto the central object, more and more magnetic flux is left behind. Indeed, by the time shown in Figs. 4 and 5, about half of the total magnetic flux of the initial core is confined within the shock radius  $r_s \sim 8 \times 10^{15}$  cm. The postshock region, which contains a small fraction ( $\sim 4\%$ ) of the total mass, is so strongly magnetized that it becomes highly magnetically subcritical (with a local dimensionless mass-to-flux ratio  $\lambda$  well below unity) even though the whole core was significantly magnetically supercritical to begin with; the small infall speed (much below free fall value) and nearly vanishing rotation speed indicate that the material in the region is essentially magnetically supported. The strong postshock field is only part of the reason for

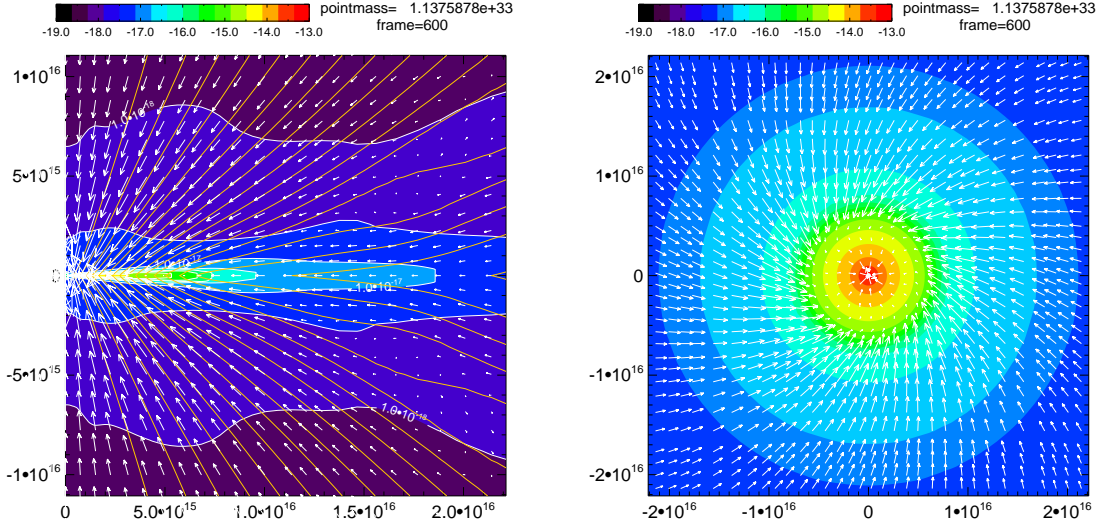


Fig. 4.— Density distribution (color map) and velocity field (white arrows) of the reference model (Model REF) in the meridian (left panel) and equatorial (right panel) planes, at a representative time  $t = 6 \times 10^{12}$  s. The highly flattened, dense equatorial structure is not a rotationally supported disk, but rather a magnetically supported, nearly non-rotating pseudodisk. Also plotted in the left panel are poloidal field lines, with the same magnetic flux between adjacent lines. The color bars above the panels are for  $\log(\rho)$ , with  $\text{g cm}^{-3}$  and cm as the units for  $\rho$  and length.



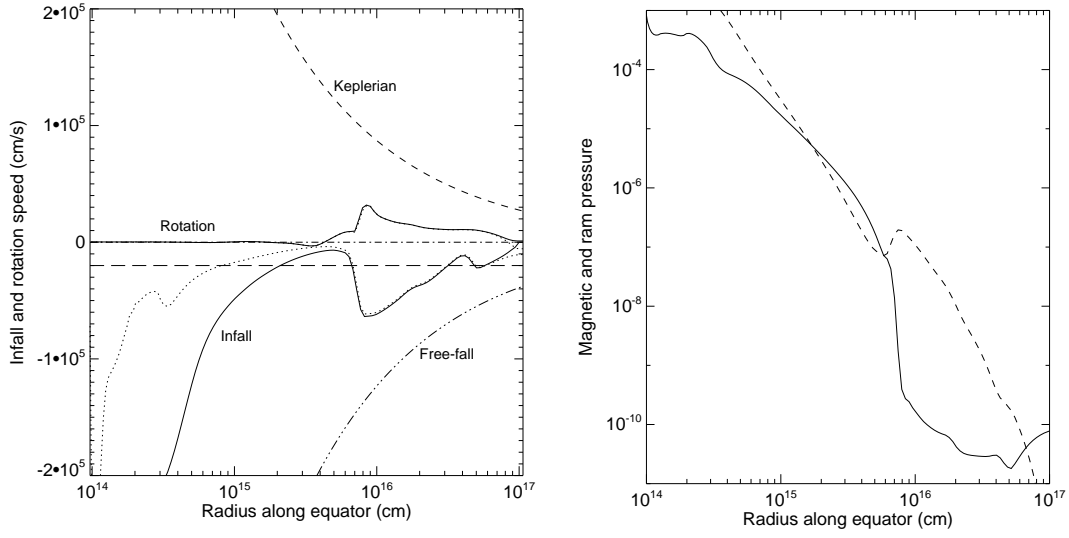


Fig. 5.— Left panel: equatorial infall (lower solid curve) and rotation (upper solid) speed for the bulk neutral material in the reference model (Model REF) at  $t = 6 \times 10^{12}$  s. Also plotted for comparison are the Keplerian speed (upper dashed) and free fall speed (lower dash-dotted) based on the central mass, the sound speed (horizontal dashed line), and zero speed line. The rapid deceleration of infalling material near the radius  $\sim 8 \times 10^{15}$  cm corresponds to a C-shock induced by ambipolar diffusion. The “effective ion speeds” defined in eq. (4) are shown as dotted lines. Right panel: magnetic (solid line) and infall ram pressure (dashed) along the equator in cgs units, showing a rapid increase in field strength near the AD shock and a corresponding drop in ram pressure.

efficient braking. Another part is that the postshock field naturally bends outwards due to strong equatorial pinching (see the left panel of Fig. 4), which increases its lever arm and thus the braking efficiency.

Even though the equatorial rotation speed at small radii remains close to zero at late times (as shown in Figs. 4 and 5), it does reach a substantial, supersonic, value for a brief period of time during the transition from the phase of prestellar collapse to the protostellar accretion phase. Fig. 6 displays the equatorial infall and rotation speeds during the transition, for 6 times separated by  $\Delta t = 4 \times 10^{10}$  s. At the earliest of the times shown, the material at small radii remains static, as expected during the pre-stellar phase of core evolution for the region within one thermal Jeans length of the origin. When the central Jeans length shrinks to inside our inner boundary, rapid protostellar accretion ensures, leading to a quick spin-up of the collapsing material. The rotation speed reaches a value as high as  $\sim 1 \text{ km s}^{-1}$  (or  $\sim 5$  times the sound speed) near the inner boundary before decreasing back again. The rapid, transient spin-up is a feature that is not captured by the self-similar solutions of Krasnopolsky & Königl (2002) and Mellon & Li (2009). The spindown is clearly associated with the development of an ambipolar diffusion induced accretion shock (see the curves for infall speed), which strengthens as it propagates outward. The material in the post-shock region is so strongly braked that it rotates backwards for a short period of time, before settling down to the nearly non-rotating state shown in Figs. 4 and 5. The strong magnetic braking prevents any rotationally supported disk larger than  $10^{14}$  cm (the size of our inner boundary) from forming at any time during our (long) simulation, which lasted until  $t = 9 \times 10^{12}$  s, when 90% of the core mass has been accreted by the central object.

### 3.2. Pure AD Runs: Grain Size, Cosmic Ray Ionization and Rotation Rates

In the reference model, the magnetic braking has clearly suppressed the formation of a rotationally supported disk (although a highly flattened, dense, magnetically supported, nearly non-rotating pseudodisk was formed). In this subsection, we explore how robust this result is, by varying the physical quantities that may affect disk formation in a lightly ionized, rotating, magnetized molecular cloud core. These include the grain size distribution and cosmic ray ionization rate, both of which affect the charge densities and thus the degree of coupling between the magnetic field and the bulk neutral matter, as well as the rate of core rotation. We discuss models where these quantities are varied over a reasonable range (see Table 1).

As discussed in §2.3, the size distribution of the grains in dense cores of molecular clouds is uncertain. We have adopted in our reference model the standard power-law MRN

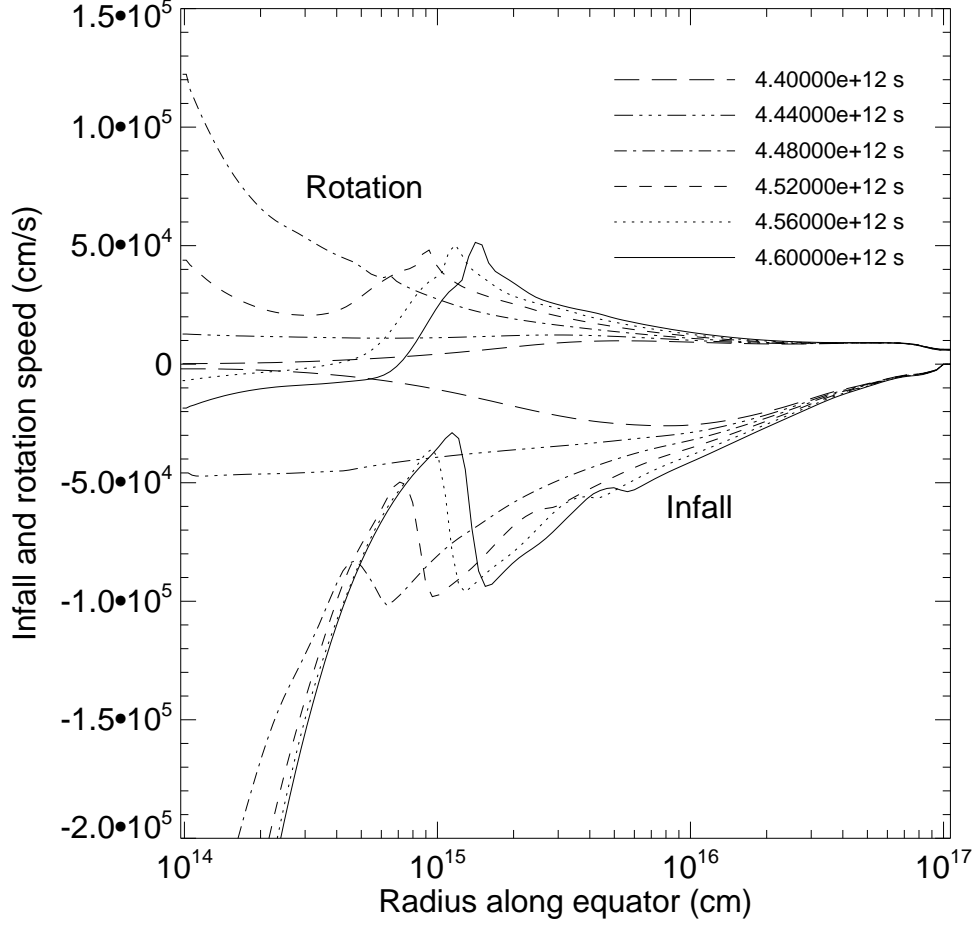


Fig. 6.— Infall and rotation speeds along the equator for the reference model (Model REF) during the transition from the pre-stellar phase of core evolution to the protostellar accretion phase, between  $t = 4.4 \times 10^{12}$  and  $4.6 \times 10^{12}$  s, showing the development of the AD shock (lower curves) and the associated strong braking of the post-shock material (upper curves).

distribution that includes a large amount of small grains. In this subsection, we will consider an opposite limit, Model LG in Table 1, where all grains are assumed to be  $1\,\mu\text{m}$  in size and the small grains are completely absent. Besides grain size, the charge densities are also affected by the cosmic ray ionization rate  $\zeta$ . Padovani et al. (2009) compiled from the literature the values of  $\zeta$  inferred for clouds of a wide range of column densities, from diffuse clouds to massive protostellar envelopes (see their Fig. 15). Most of the inferred values are above our reference value  $\zeta = 10^{-17}\,\text{s}^{-1}$ , although there are a few exceptions. We will consider a model with  $\zeta = 10^{-18}\,\text{s}^{-1}$  (Model LoCR in Table 1), which is a lower limit to the inferred values. For illustration, we will also consider a case with a higher rate  $\zeta = 3 \times 10^{-17}\,\text{s}^{-1}$  (Model HiCR), close to the value inferred by Webber (1998) for the local interstellar medium. In addition, we consider the effect of varying the core rotation rate  $\Omega_0$ . Our reference value  $\Omega_0 = 10^{-13}\,\text{s}^{-1}$  corresponds to a ratio of rotational to gravitational binding energy of  $\beta = 0.025$ , which is typical of the cores discussed in Goodman et al. (1993). A spread exists for the inferred  $\beta$  values, which motivates us to consider two additional rotation rates:  $\Omega_0 = 5 \times 10^{-14}$  (Model LoROT) and  $2 \times 10^{-13}\,\text{s}^{-1}$  (Model HiROT), corresponding to  $\beta = 0.006$  and  $0.1$ , respectively.

The different variants of the reference model are compared in Fig. 7, which plots the infall and rotation speeds on the equator at a common time  $t = 5.5 \times 10^{12}\,\text{s}$  for all models except Model HiROT (which has yet to form a central object at this time, because the collapse is significantly delayed by the combination of a moderately strong magnetic field and fast rotation). The most striking feature of Fig. 7 is that the rotation speed is essentially zero at small radii (within  $\sim 10^{15}\,\text{cm}$ ) for all of the models shown. The same is true for Model HiROT (not shown in the figure) at later times (greater than  $\sim 6.2 \times 10^{12}\,\text{s}$ ), when the fast rotating core has collapsed. Apparently the magnetic braking is strong enough to remove essentially all of the angular momentum of the equatorial material inside the AD shock for the realistic ranges of grain size distribution, cosmic ray ionization rate and core rotation rate explored here.

Suppression of RSD in some cases is easy to understand. The elimination of small grains in Model LG and the higher cosmic ray ionization rate in Model HiCR increase the densities of electrons and ions, which strengthens the coupling between the magnetic field and the bulk neutral matter. Since a better magnetic coupling is expected to make the braking more efficient, it is not surprising to find that the RSD remains suppressed as in the reference model. In these two cases, the AD shock is located at a slightly smaller radius compared with the reference case (see Fig. 7). We interpret this effect as a result of the better coupling, which forces the bulk neutral material to collapse more slowly, which in turn leads to a somewhat lower central mass ( $8.62 \times 10^{32}\,\text{g}$  for Model LG and  $8.69 \times 10^{32}\,\text{g}$  for Model HiCR) than in the reference model at the same time ( $9.29 \times 10^{32}\,\text{g}$ ). Associated

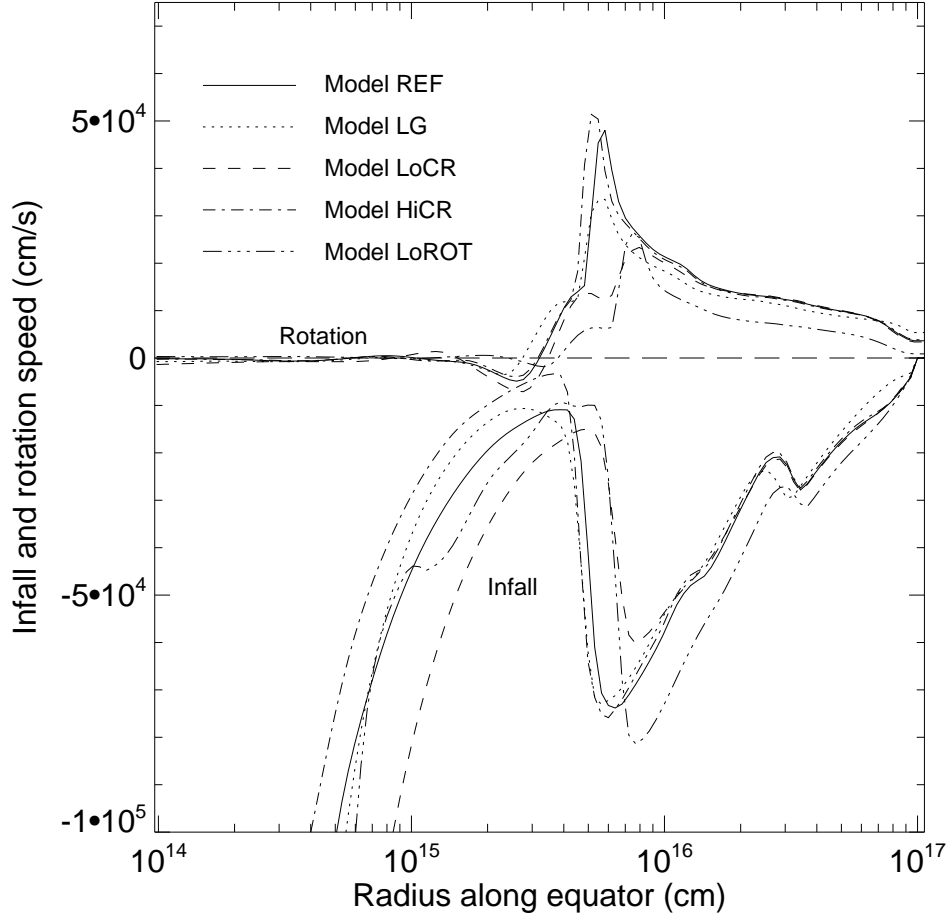


Fig. 7.— Comparison of the infall and rotation speeds along the equator for variants of the reference model with different grain size distribution (Model LG), cosmic ray ionization rate (Models LoCR and HiCR), and rotation rate (Model LoROT), at a representative time  $t = 5.5 \times 10^{12}$  s. The nearly zero rotating speed at small radii indicates the absence of a rotationally supported disk due to efficient magnetic braking for all cases shown.

with the lower mass is a lower magnetic flux accumulating outside the central object, which drives a smaller AD shock.

The situation with Model LoCR is the opposite. The lower cosmic ray ionization rate decreases the degree of ionization in the core, which weakens the coupling between the magnetic field and the bulk neutral matter. The weakening of magnetic coupling is expected to reduce the braking efficiency in principle. The braking is not weakened enough, however, to enable an RSD to form, as evidenced by the vanishing rotation speed and fast infall inside the AD shock. In this case, the shock radius is somewhat larger than that of the reference model (see Fig. 7), because of a faster post-shock infall, which leads to a larger central mass ( $9.76 \times 10^{32}$  g for Model LoCR) and thus a larger left-behind magnetic flux for shock driving.

Neither Model LoROT nor HiROT produced a rotationally supported disk. The former is to be expected, since the angular momentum is lower for a more slowly rotating core, and should be easier to remove by magnetic braking. The slower rotation also presents a lesser obstacle to the collapse, allowing the formation of a larger central mass ( $1.24 \times 10^{33}$  g) and a larger AD shock (see Fig. 7) than in the reference model at the same time. In the opposite case of HiROT, the stronger rotational support delayed the formation of a central object until a much later time. Once the central object has formed, magnetic braking is again strong enough to remove essentially all of the angular momentum from the material near the central object, preventing an RSD from forming during the protostellar accretion phase.

We conclude that disk formation is suppressed by a moderately strong magnetic field in the presence of ambipolar diffusion for the range of parameters that we consider realistic.

### 3.3. Ohmic Dissipation

How does the Ohmic term in the induction equation (1) affect the core collapse and disk formation? To address this question, we repeat the reference model, but with the Ohmic dissipation included (Model REF<sub>AO</sub> in Table 1) in addition to the ambipolar diffusion (although not yet the Hall term, see below). It turns out that the Ohmic dissipation modifies the dynamics of the core collapse and protostellar accretion relatively little, as can be seen from Fig. 8, which compares the equatorial infall and rotation speeds of Model REF<sub>AO</sub> and the reference model at four representative times. The speeds for the two cases are barely distinguishable over most of the space. The conclusion is that in the presence of ambipolar diffusion, Ohmic dissipation does not enable the formation of RSD.

The reason that Ohmic dissipation is ineffective in modifying the flow dynamics in

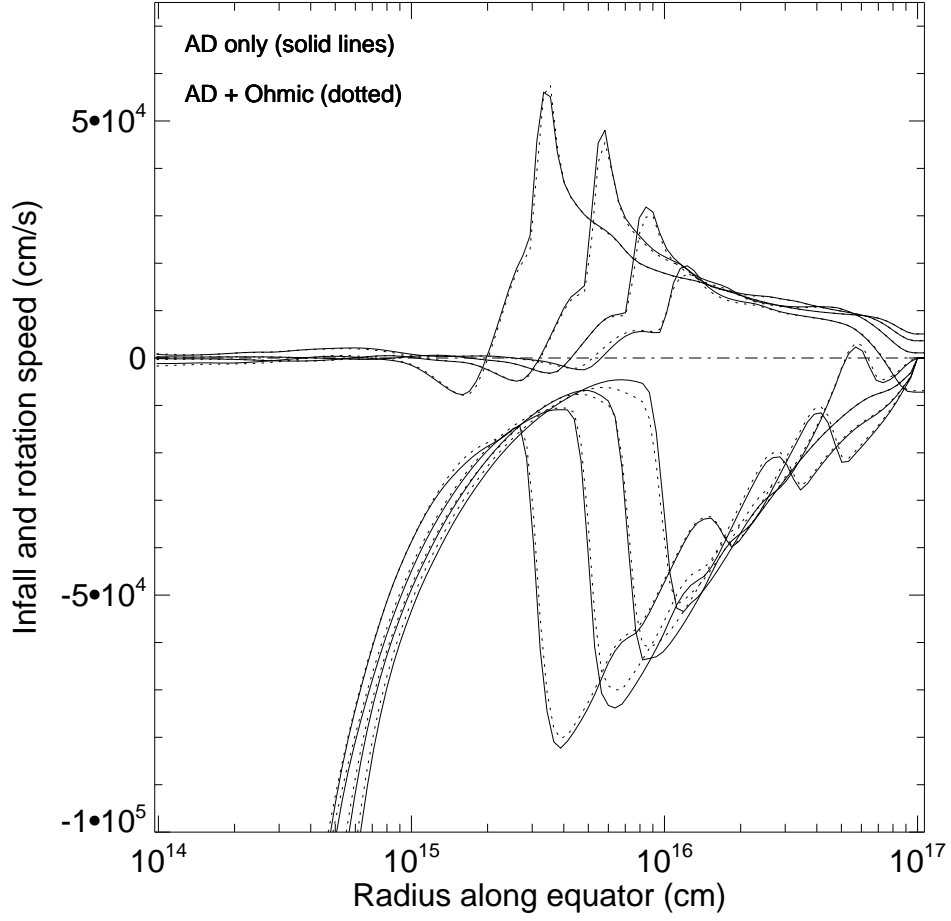


Fig. 8.— Comparison of the infall and rotation speeds along the equator for Model  $\text{REF}_{AO}$  (with both ambipolar diffusion and Ohmic dissipation; dotted lines) to the reference model (with only ambipolar diffusion; solid), at representative times  $t = 5 \times 10^{12}$ ,  $5.5 \times 10^{12}$ ,  $6 \times 10^{12}$ , and  $6.5 \times 10^{12}$  s. The similarity between the two sets of curves shows that Ohmic dissipation does not affect the flow dynamics much.



the presence of ambipolar diffusion is simple: the Ohmic diffusivity  $\eta_O$  is smaller than the ambipolar diffusivity  $\eta_A$  by more than an order of magnitude (see Fig. 9). The relatively small Ohmic diffusivity is a result of the relatively low density in the computational domain, with  $\rho \lesssim 10^{-13} \text{ g cm}^{-3}$  (or  $n_H \lesssim 4 \times 10^{10} \text{ cm}^{-3}$ ) typically. The moderate density is a result of strong magnetic braking, which yields a relatively low-density, collapsing pseudodisk (rather than a denser, well supported RSD) in the equatorial region.

Even when ambipolar diffusion is turned off, we do not find any rotationally supported disk within our computation domain (outside a radius of  $10^{14} \text{ cm}$ ) that is resulted from Ohmic dissipation (Model REF<sub>O</sub> in Table 1). Indeed, the overall flow dynamics in the pure Ohmic case is strikingly similar to the reference case that has only ambipolar diffusion (compare Fig. 10 to Fig. 4). The reason for the similarity is that Ohmic resistivity does not destroy the *net* magnetic flux that passes from one hemisphere to the other through the equatorial plane (because the poloidal field lines are tied to the low density regions well above and below the equatorial plane where Ohmic dissipation is negligibly small; see discussion in Shu et al. 2006). Rather, it enables the poloidal field lines to diffuse radially outward, similar to ambipolar diffusion. As more and more matter accretes across the field lines into the center, the left-behind magnetic flux piles up at small radii, as shown in the left panel of Fig. 10. The flux pile-up is qualitatively similar to the pure-AD reference case (see the left panel of Fig. 4). It leads to a strongly magnetized equatorial region where the infall speed decreases to well below the free-fall value and the rotation is almost completely braked (see the right panel of Fig. 10). We have repeated the Ohmic dissipation-only calculation with a reduced radius for the inner boundary (from  $10^{14} \text{ cm}$  to  $3 \times 10^{13} \text{ cm}$  or 2 AU), and found the same result: namely, a realistic level of (classical) Ohmic resistivity is not large enough to enable the formation of rotationally supported disks larger than several AUs, at least in 2D (axisymmetry). This is in agreement with Krasnopolsky et al. (2010), who showed that enhanced resistivity is needed for such disks to form.

### 3.4. Hall Effect

Under the conditions encountered in our core collapse calculations, the magnitude of the Hall diffusivity in the induction equation (1) is typically larger than the Ohmic diffusivity (see Fig. 3). We therefore expect the Hall term to have a larger effect on the collapse dynamics than the Ohmic term discussed in the last subsection. We find that this is indeed the case. Fig. 11 plots the infall and rotation speeds on the equator for Model REF<sub>AHO</sub><sup>−</sup>, which includes all three nonideal MHD terms in equation (1) and an initial magnetic field that points in a direction opposite to the initial rotation axis (in the negative “z” direction, and hence the

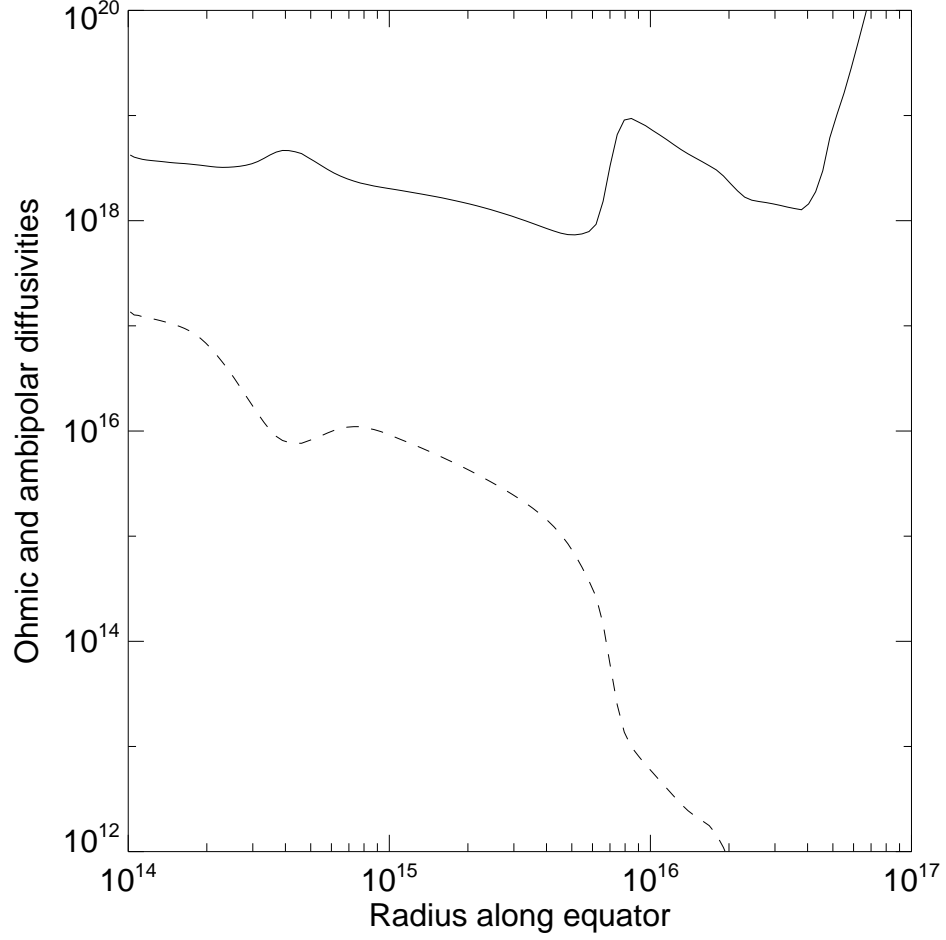


Fig. 9.— Comparison of the Ohmic diffusivity (dashed line) and the ambipolar diffusivity (solid) along the equator for Model  $\text{REF}_{AO}$  (with both ambipolar diffusion and Ohmic dissipation) at a representative time  $6 \times 10^{12}$  s. The large difference between the two indicates that the Ohmic dissipation is relatively unimportant.

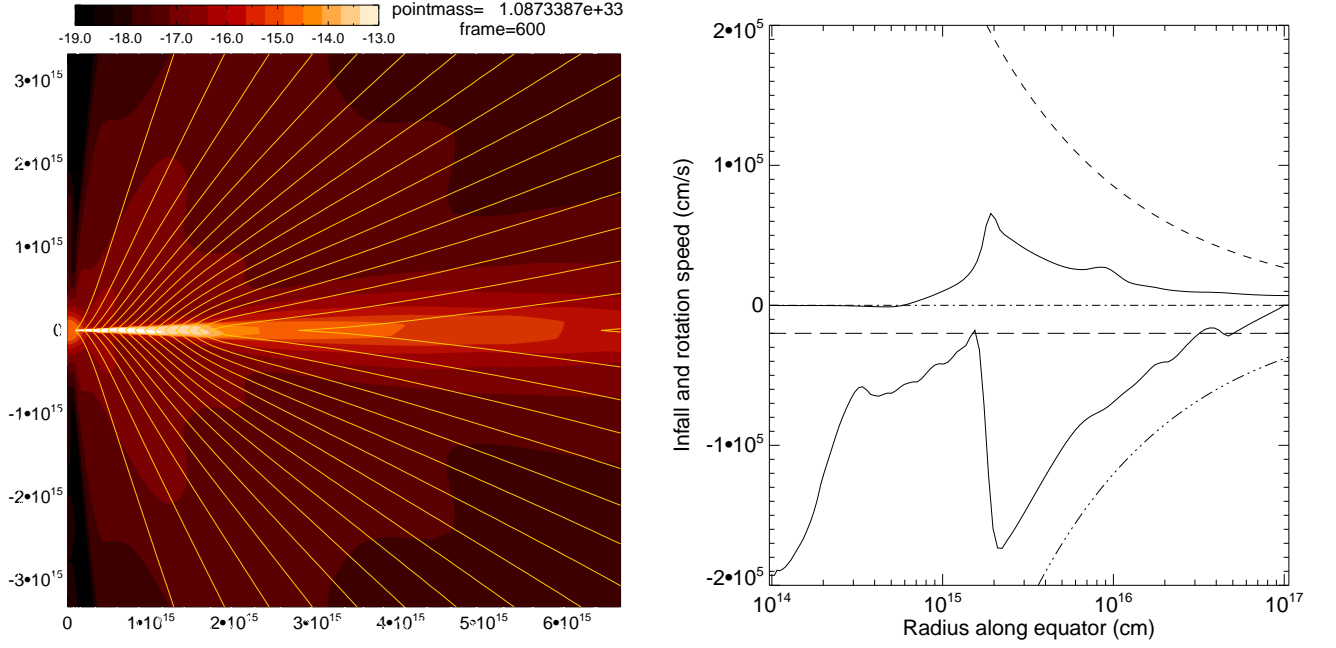


Fig. 10.— Density map with field lines (left panel) and equatorial infall and rotation speed (right) for Model  $\text{REF}_O$  (with Ohmic dissipation only) at  $t = 6 \times 10^{12}$  s. Also plotted for comparison in the right panel are the Keplerian speed based on the central mass (upper dashed curve), free fall speed (lower dash-dotted curve), sound speed (horizontal dashed line), and zero speed line. Note the rapid deceleration of infalling material near the radius  $\sim 2 \times 10^{15}$  cm. It is caused by magnetic flux pileup at small radii due to Ohmic diffusion, similar to the AD shock shown in Figs. 4 and 5.

superscript “-” in the model name). Plotted are the speeds during the transition from the pre-stellar core evolution to the protostellar accretion phase, as in Fig. 6 for the reference (AD only) model. Comparing Figs. 11 and 6 reveals that the Hall term has relatively little effect on the equatorial infall speed. In both cases, as more and more mass accumulates at the center, an AD shock develops where the collapsing material slows down temporarily, before reaccelerating towards the origin. The effect on the rotation speed is much more pronounced. The Hall effect enabled the equatorial material in the post-AD shock region to rotate faster compared to the reference case. The difference is especially clear at later times, when the rotation inside the AD shock is almost completely braked (or even reversed) by magnetic braking in the reference case. In the presence of the Hall effect, the post-shock material rotates at a speed as high as 5 times the sound speed. The rotation speed remains much smaller than the Keplerian speed, however, indicating that a rotationally supported disk is not enabled by the Hall effect. The lack of an RSD is also evident from the fact that the post-shock region collapses at a high speed at small radii.

The significant Hall effect on the post-shock rotation speed can be understood as follows. The Hall effect depends on the current density  $\mathbf{j}$  ( $\propto \nabla \times \mathbf{B}$ ; see eq. [1]), which is predominantly in the toroidal direction because of strong magnetic field pinching in the equatorial region. It is particularly strong in the equatorial post-shock region, where the field is strong and is bent outward significantly (see the left panel of Fig.4). The toroidal current drives a twist of the field lines in the azimuthal direction, which in turn generates a torque that acts to spin up the post-shock material.

An interesting feature, pointed out for example in the disk-wind study of Wardle & Königl (1993), is that when the field direction is reversed, the torque induced by the Hall effect changes direction as well (Krasnopolsky et al. 2011). This is illustrated in Fig. 12. Whereas the reference model has a post-shock region nearly completely braked in the absence of the Hall effect, both Model  $\text{REF}_{\text{AHO}}^+$  and Model  $\text{REF}_{\text{AHO}}^-$  have substantial, supersonic rotation in the post-shock region, although in opposite directions. In particular, in Model  $\text{REF}_{\text{AHO}}^+$  where the initial magnetic field is aligned (rather than anti-aligned) with the initial rotation axis, the magnetic torque induced by the Hall effect has forced the equatorial material at small radii to rotate in a direction opposite to the material at larger distances; the resultant shear may induce instabilities in 3D that should be investigated in the future. The change in the direction of the torque from Model  $\text{REF}_{\text{AHO}}^-$  to Model  $\text{REF}_{\text{AHO}}^+$  is due to the change in the poloidal field direction which, for the same outward bending of field lines, produces a flip in the direction of the toroidal current. Nevertheless, in neither field orientation was the Hall spin-up strong enough to produce a rotationally supported disk, as evidenced by the rapid infall speed at small radii where the rotation speed is relatively high (but still well below the local Keplerian speed). Indeed, there is relatively little change in the infall speed

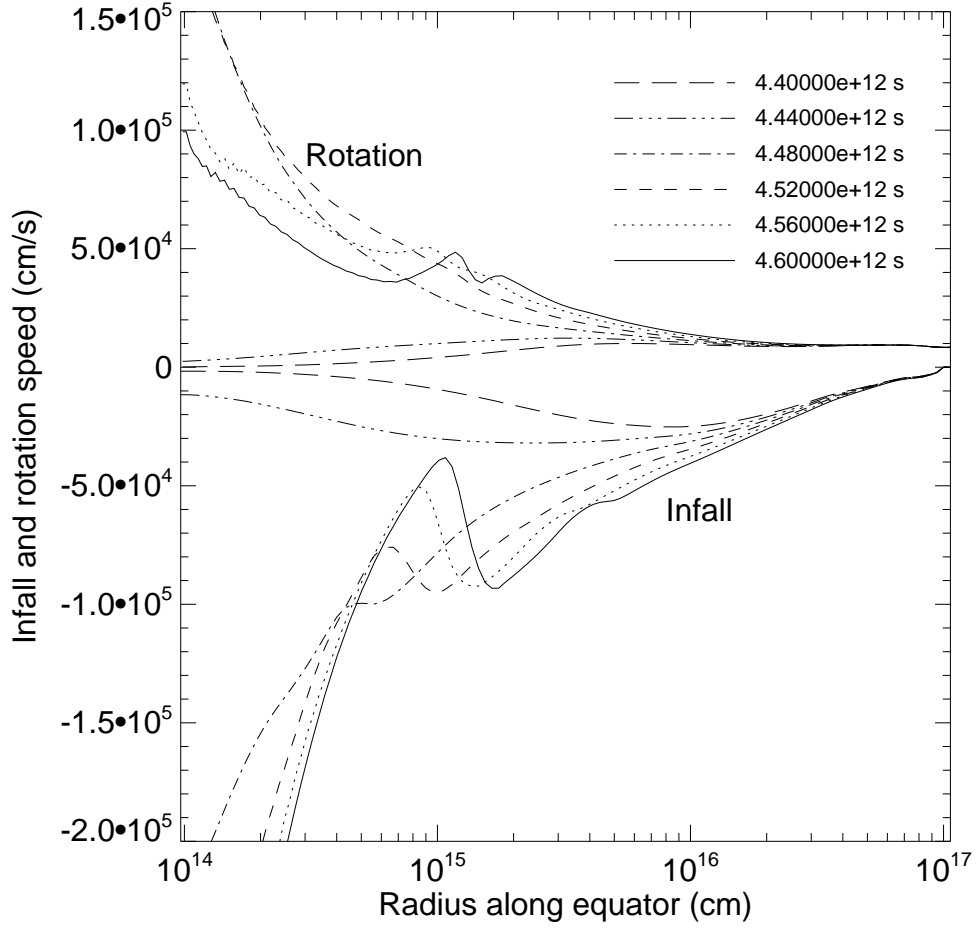


Fig. 11.— Infall and rotation speeds along the equator for Model REF<sub>AHO</sub><sup>−</sup> (including all three non-ideal MHD terms) during the transition from the pre-stellar core evolution phase to the protostellar accretion phase, between  $t = 4.4 \times 10^{12}$  and  $4.6 \times 10^{12}$  s, as in Fig. 6. The Hall effect enables the material at small radii inside the AD shock to rotate at supersonic values.

with or without the Hall effect, because the radial current density is relatively small, making the Hall effect less important in that direction.

We will return to the Hall effect in section 5, where we consider the simpler case of the collapse and spin-up of an initially non-rotating core due to Hall effect.

#### 4. Weak Magnetic Fields and Potential Disk Formation

We now consider cases with a weak initial magnetic field of  $B_0 = 10.6 \mu\text{G}$  (at an initial molecular hydrogen density of  $n_{H_2} = 10^5 \text{ cm}^{-3}$ ), which is 30% of the reference value. It corresponds to a dimensionless mass-to-flux ratio of  $\lambda = 9.73$  for the core as a whole, and  $\lambda_c = 14.6$  on the central magnetic flux tube. If the dense core were to condense more or less isotropically out of a more diffuse material of  $10^{3.5} \text{ cm}^{-3}$  in density under the flux freezing condition, it would require only an unrealistically weak field of  $1.06 \mu\text{G}$  in the diffuse gas for the core to have  $B_0 = 10.6 \mu\text{G}$ . For this reason, we believe that this value of  $B_0$  is probably as low as, if not lower than, the minimum field strength that can be reasonably expected in the type of dense cores under consideration.

Weaker fields are expected to be less efficient in magnetic braking. This is because the braking rate involves the product of the toroidal and poloidal field strengths, and thus generally scales with the field strength as  $B^2$ . Indeed, for Model WREF which has the same parameters as the reference model (Model REF) except for a weaker field of  $B_0 = 10.6 \mu\text{G}$ , a small ( $\sim 20 \text{ AU}$ ) rotationally supported disk is formed temporarily early in the protostellar accretion phase, around the time  $t \sim 3.68 \times 10^{12} \text{ s}$ , when the central mass is only  $\sim 0.07 M_\odot$ . This disk disappears at later times, however, because of strong magnetic braking, which drives a powerful outflow before the disk disappears (see Shang et al., in preparation).

The suppression of the rotationally supported disk at later times is illustrated in Fig. 13. It includes a snapshot of the collapsing core (left panel) and a plot of the equatorial infall and rotation speeds (right panel), at  $t = 5 \times 10^{12} \text{ s}$  when the central mass is  $0.29 M_\odot$ . At this time, the prominent polar outflow at the earlier times has disappeared. It is replaced by a polar region of strong infall, mostly along the magnetic field lines. The lack of outflow indicates the rotating disk that drives the outflow no longer exists. The disk suppression is shown clearly in the equatorial rotation speed, which is close to zero inside the AD shock (around  $10^{15} \text{ cm}$ ). The rapid, supersonic infall at small radii further supports the lack of an RSD, as in the more strongly magnetized standard model (see Fig. 4 and 5).

Disk suppression is not unique to Model WREF. In the left panel of Fig. 14 we show three additional examples (Models WLG, WHiCR and WLoROT in Table 1), where the disk

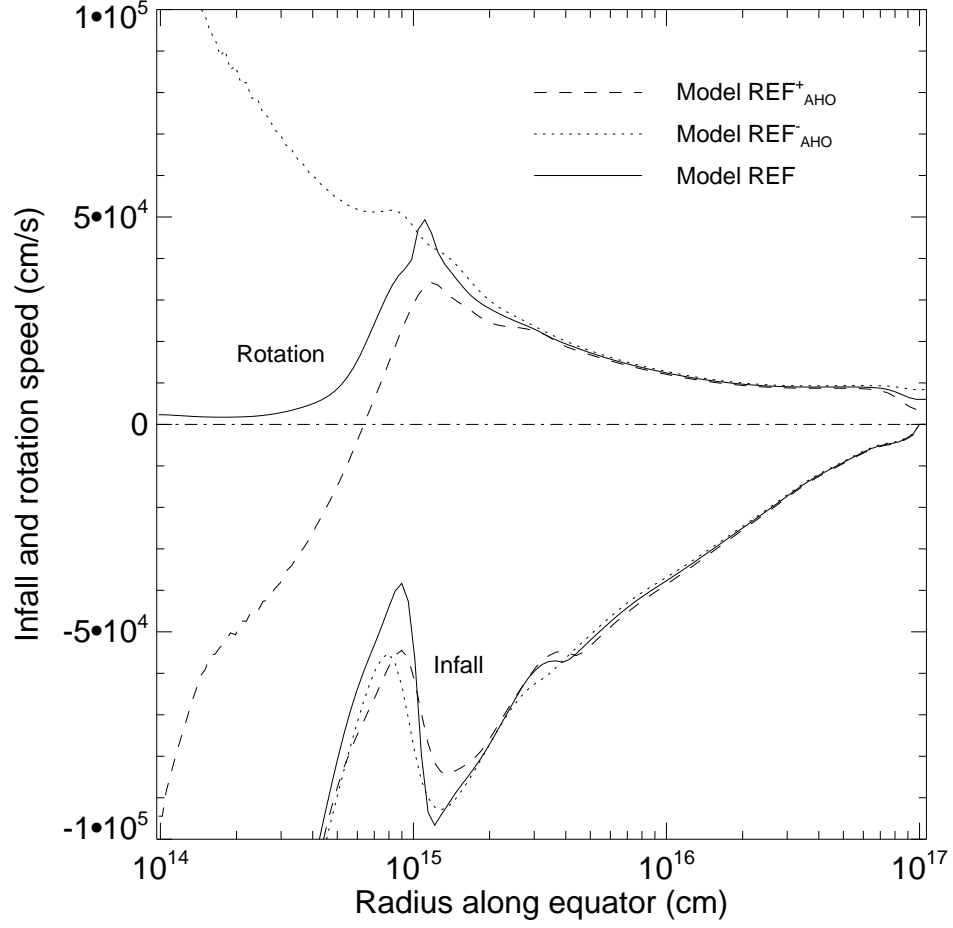


Fig. 12.— Infall and rotation speeds along the equator for two models of opposite initial magnetic orientation, Model REF<sub>AHO</sub><sup>+</sup> (dashed lines) and Model REF<sub>AHO</sub><sup>-</sup> (dotted), at  $t = 4.55 \times 10^{12}$  s. The reference model (solid) without the Hall effect is also plotted for comparison.



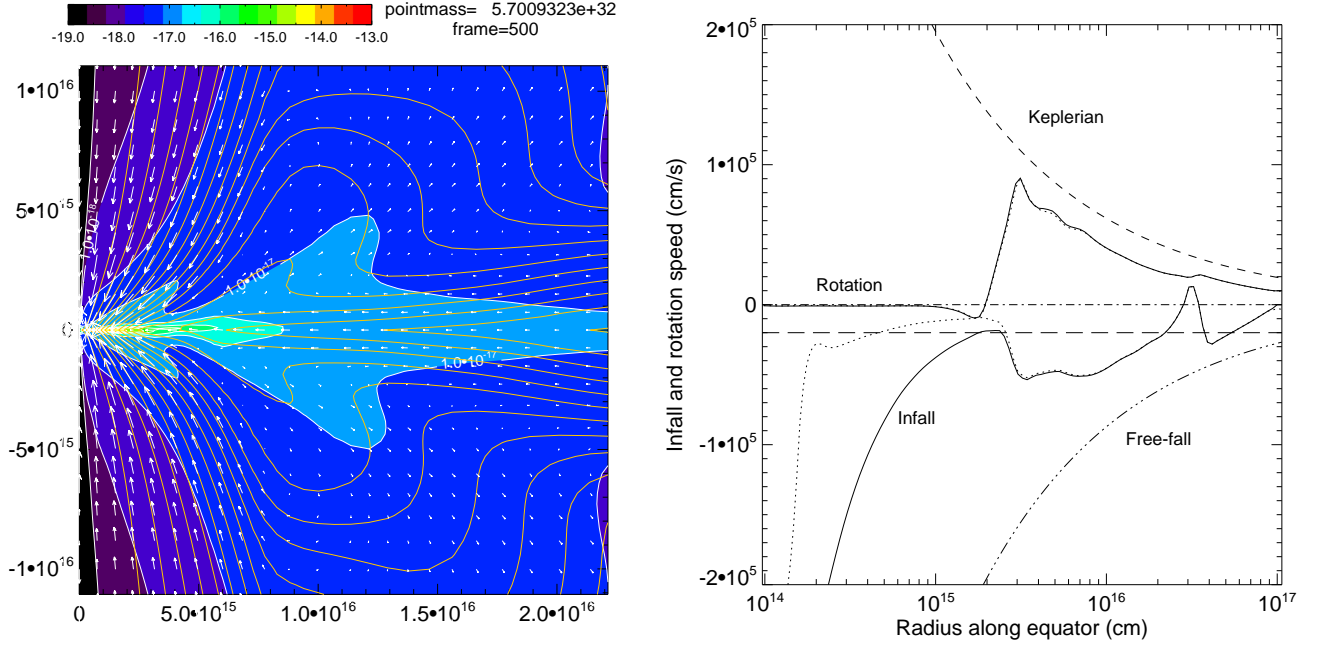


Fig. 13.— Density color map, velocity field (white arrows) and magnetic field lines (yellow) of the collapsing core (left panel) and equatorial infall and rotation speeds (right panel) for the standard weak magnetic field model (Model WREF) at a relatively late time  $t = 5 \times 10^{12}$  s, showing that the RSD formed earlier has by now completely disappeared. Also plotted for comparison in the right panel are the Keplerian speed (upper dashed) and free fall speed (lower dash-dotted) based on the central mass, the sound speed (horizontal dashed line), and zero speed line. The “effective ion speeds” defined in eq. (4) are shown as dotted lines.

formation is suppressed at a relatively late time  $t = 5 \times 10^{12}$  s, when the central mass is 0.40, 0.34 and  $0.65 M_{\odot}$ , respectively. These models have the same weak magnetic field as Model WREF, but have either a larger grain size (Model WLG), a higher cosmic ray ionization rate (Model WHiCR), or a lower initial rotation rate (Model WLoROT). The lack of disk is not too surprising for Models WLG and WHiCR, because the magnetic fields are better coupled to the neutral matter in these models than in Model WREF. The absence of a disk in Model WLoROT is also expected, because its more slowly rotating core is more easily braked.

Some rotationally supported disks do form with other choices of parameters, however, at least at early times. The disk formation is illustrated in the right panel of Fig. 14, where the equatorial infall and rotation speeds for Models WLoCR (same as the standard weak field model but with a lower cosmic ray ionization rate), WHiROT (with a higher initial core rotation rate) and VWREF (with an unrealistically low  $B_0 = 3.54 \mu\text{G}$ ) are plotted at a early time, when the central mass is only  $1.79 \times 10^{-2}$ ,  $1.27 \times 10^{-2}$  and  $1.05 \times 10^{-2} M_{\odot}$ , respectively. There is more mass in the rotationally supported disk than at the center, which is why the rotation curve is non-Keplerian except close to the origin. Each of the disks drives a strong, sometimes chaotic, outflow, which makes it hard to continue the non-ideal MHD simulation reliably to much later times. The disk in the weakest field case (Model VWREF) evolves into a ring, which may fragment in 3D. It is unclear whether the early disk in the other two cases can survive subsequent magnetic braking or not (it did not in the standard weak field model WREF). Once a disk becomes self-gravitating, gravitational torque will likely become important in the disk dynamics. This important effect is not captured in our axisymmetric simulations. In any case, it is clear that disk formation in the moderately weak magnetic field case is more complicated than the moderately strong field case, with the outcome depending on the core rotation rate and the degree of field-matter coupling, at least at early times. Paradoxically, the weaker field cases are more difficult to simulate because of strong, chaotic outflows. More work is needed before firmer conclusions on disk formation can be drawn.

## 5. Hall Spin-up of Non-Rotating Envelope

Of the three non-ideal MHD effects, the Hall effect is the least explored in the context of core collapse and disk formation (see, however, Krasnopolsky et al. 2011 and C. Braiding 2011). We have seen in §3.4 that it can spin up the nearly completely braked post-AD shock material in an initially rotating core to a significant speed, and the sense of the Hall-induced rotation depends on the orientation of the magnetic field. This Hall spin-up can be illustrated even more clearly in the collapse of an initially non-rotating core, where any rotation that develops subsequently must come solely from the Hall effect.

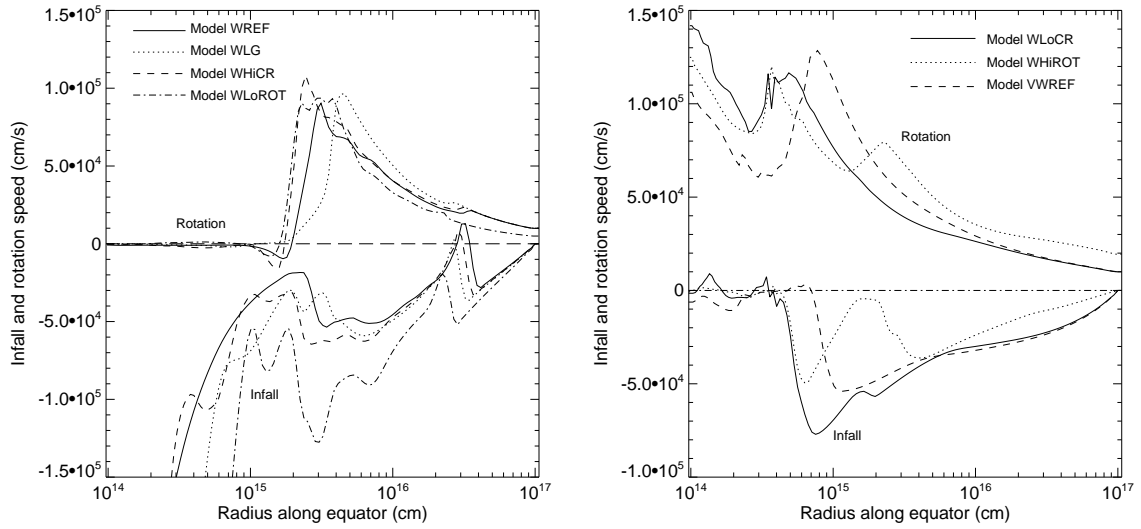


Fig. 14.— Left panel: Infall and rotation speeds on the equator for those models with a weak magnetic field that do not have a rotationally supported disk at a relative late time  $t = 5 \times 10^{12}$  s. Right panel: Same as the left panel but for those models that do have what appear to be the rotationally supported disks at early times, when the central mass is only  $\sim 1\%$  of the core mass. Whether these (small) disks can survive to much later times or not is unclear.

We will concentrate on Model NoROT $_{AHO}^-$  where all three non-ideal MHD effects are included and the initial magnetic field is anti-parallel to the rotation axis. We have confirmed that the case with opposite field orientation (Model NoROT $_{AHO}^+$ ) produces identical results, except that the sign of the Hall-induced rotation is flipped, as expected. The left panel of Fig. 15 gives an overall impression of the Hall-induced rotation on an intermediate scale of  $\sim 10^{16}$  cm, at a representative time  $t = 4.4 \times 10^{12}$  s, when the central mass is  $0.26 M_{\odot}$ . Note the alternating pattern of negative and positive rotation speeds, with maximum values reaching  $\sim 10^5 \text{ cm s}^{-1}$ , which is much higher than the sound speed ( $2 \times 10^4 \text{ cm s}^{-1}$ ). On smaller scales, the structure is dominated by a dense flattened pseudodisk that is visible from the iso-density contours in Fig. 15.

The dense equatorial pseudodisk is collapsing as well as spinning in the positive azimuthal direction, as shown pictorially in the right panel of Fig. 15 and more quantitatively in the left panel of Fig. 16. The collapse shows rapid deceleration near  $\sim 2 \times 10^{15}$  cm and reacceleration interior to it, characteristic of an AD shock. The infall speed is similar to that in the pure-AD case, indicating that the Hall effect modifies relatively little the overall collapse dynamics. The difference in rotation speed is more pronounced, especially in the post-shock region, where the maximum rotation speed exceeds  $10^5 \text{ cm s}^{-1}$ , comparable to the peak value on the large scale shown in Fig. 15. The rotational component of the “effective ion speed” (defined in equation [4]) is larger than the neutral rotation speed, indicating that a magnetic force is exerted in the positive azimuthal direction to drive the ion-neutral drift. It is the same force that torques up the pseudodisk. The force is particularly large in the postshock region, because the magnetic field is strong there. Nevertheless, the spin up fails far short of reaching a Keplerian rate, which is the reason why the overall collapse dynamics is little affected.

In an initially non-rotating core, any spin up in one direction must be offset by a spin up in the opposite direction, so that the total angular momentum is conserved. In the region that extends from the origin up to the AD shock, the net angular momentum is positive (see the right panel of Fig. 16), because it is dominated by the positively spinning pseudodisk. Outside the AD shock, the net angular momentum is negative, dominated by the hour-glass shaped counter-rotating region shown in left panel of Fig. 15. One may expect the positive and negative angular momenta to sum up to zero over the entire computational volume. However, this is not the case, because the total angular momentum is dominated by the material at large distances (near the core edge) whose rotation speed is small but non-zero (see the left panel of Fig. 16). Because the mass at larger distances is larger and has a longer lever arm, it dominates the total angular momentum. The total positive angular momentum inside the computation domain is  $6.52 \times 10^{52} \text{ g cm}^2 \text{ s}^{-1}$  whereas the total negative angular momentum is  $-9.38 \times 10^{51} \text{ g cm}^2 \text{ s}^{-1}$ . They do not cancel out exactly. Some of the angular

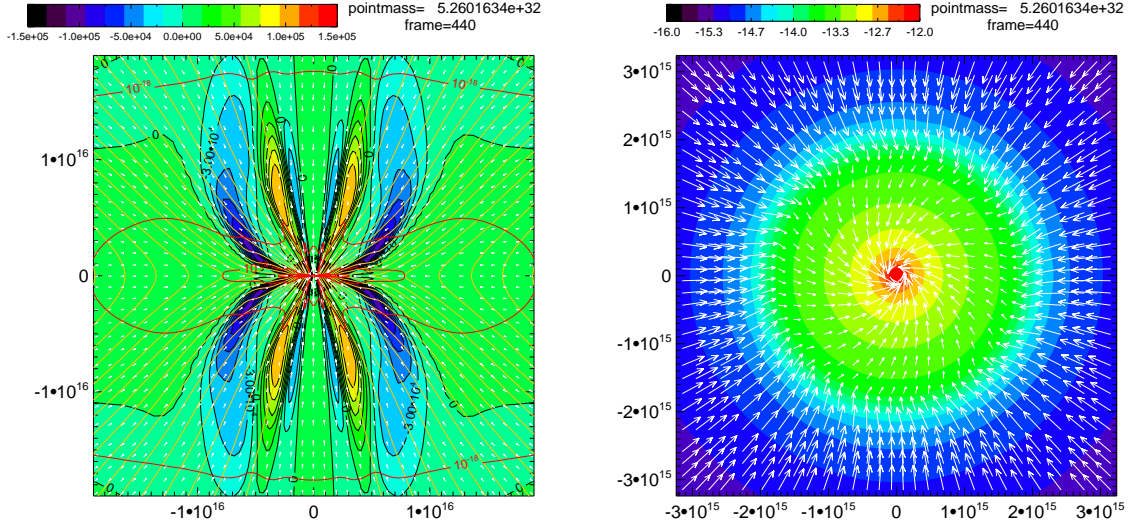


Fig. 15.— Left panel: map of the Hall-induced rotation speed during the collapse of an initially non-rotating core (Model REF<sub>AHO</sub><sup>-</sup>) at a representative time  $t = 4.4 \times 10^{12}$  s, when the central mass is  $0.26 M_{\odot}$ . Also plotted are magnetic field lines (yellow), isodensity contours (red, spaced by a factor of 10), and velocity vectors (white). Right panel: map of  $\log(\rho)$  (color) and velocity field (white vectors) in the equatorial plane, showing the spin up of the dense, post-AD shock region due to Hall effect.

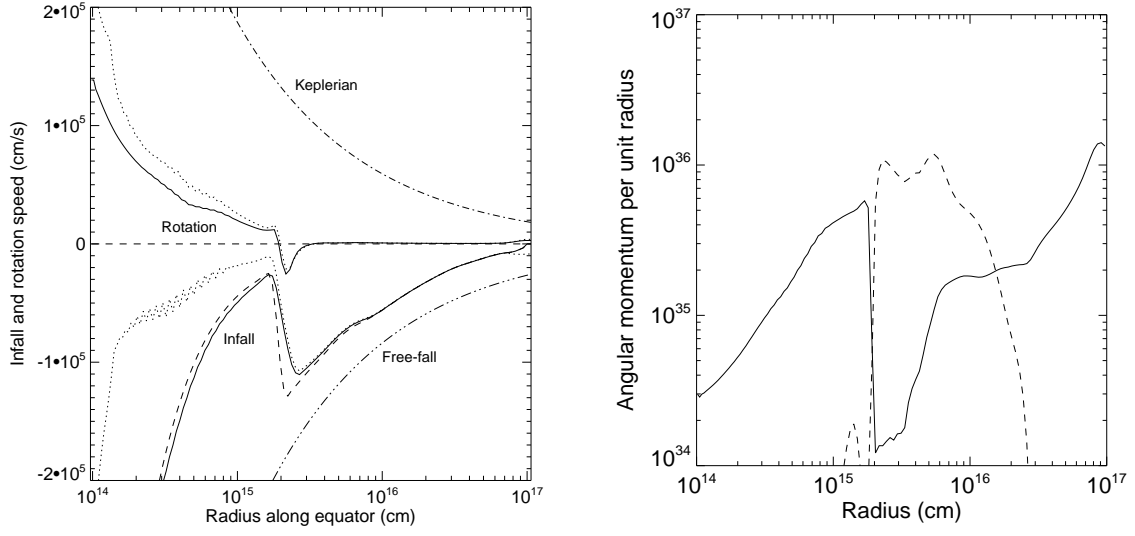


Fig. 16.— Left Panel: equatorial infall and rotation speeds of the neutral matter (solid lines) for the collapse of an initially non-rotating core. Also plotted for comparison are “effective ion speeds” (defined in equation [4], dotted lines), and the infall and rotation speeds in an AD-only case that does not have any Hall effect (dashed lines). Right panel: Positive (solid line) and negative (dashed) angular momentum per unit radius  $dL/dr$  as a function of radius.

momentum must have left the computation box, through torsional Alfvén waves. Dividing the total net angular momentum by the total mass left in the simulation box ( $1.47 \times 10^{33}$  g) yields  $3.80 \times 10^{19} \text{ cm}^2 \text{ s}^{-1}$ , which is the average specific angular momentum. For a core size of  $10^{17}$  cm, the corresponding characteristic rotation speed is  $3.8 \times 10^2 \text{ cm s}^{-1}$ , about 2% of the sound speed, much smaller than the rotation speed achieved on the  $10^{16}$  cm scale or smaller. We conclude that, despite the localized, supersonic rotation induced on small scales, the influence of the Hall effect on the global dynamics is limited.

## 6. Discussion

### 6.1. Why is Protostellar Disk Formation Difficult in Magnetized Cores?

#### 6.1.1. *Ideal MHD Limit*

The fundamental reason for the difficulty in forming protostellar disks in magnetized cores is that the protostellar collapse concentrates magnetic flux at small radii, precisely where the rotationally supported disk (RSD) tends to form in the absence of magnetic braking. The basic difficulty can be seen most clearly in the ideal MHD limit, where magnetic flux is dragged into the central star (because of flux freezing) to form a split magnetic monopole. The rapid increase in field strength towards the central object enables the (split) monopolar field to brake the circumstellar disk catastrophically, as shown analytically by Galli et al. (2006; see their Fig. 1 for a sketch of the expected field geometry).

A case can also be made for catastrophic disk braking in the ideal MHD limit from numerical simulations (Allen et al. 2003; Mellon & Li 2008; Hennebelle & Fromang 2008), although it is less clean cut. The reason is that, as the mass of the protostar grows, more and more magnetic flux is dragged to the origin, which creates a stronger and stronger (split) magnetic monopole that squeezes more and more strongly on the material on the equator from above and below. When the oppositely directed magnetic fields above and below the equator are squeezed within a single cell of each other, numerical reconnection becomes unavoidable. The expected numerical reconnection is present in the ideal MHD simulations of Mellon & Li (2008), especially for relatively strongly magnetized cores (with a dimensionless mass-to-flux  $\lambda$  of several or less; see their Figs. 14-16), where no RSDs form but the numerical results are complicated by reconnections. The collapse of more weakly magnetized cores of  $\lambda \sim 10$  is not significantly affected by reconnections, and yet no RSDs form either. The conclusion from the ideal MHD simulations is that magnetic braking is efficient enough to suppress disk formation for  $\lambda \lesssim 10$ .



The above conclusion is strengthened by the resistive MHD disk-formation calculations of Krasnopolsky et al. (2010), which included a wide range of (prescribed) resistivity. They found that, as the resistivity is decreased below a certain value, (numerical) reconnection starts to become important (as expected), which complicates the interpretation of the numerical results. However, before the reconnection sets in, the RSD is already completely braked by a moderately strong magnetic field. Extrapolating the results for those clean, low resistivity runs without numerical reconnection to the zero resistivity limit (where numerical reconnection is unavoidable) indicates that complete disk suppression also holds true for the ideal MHD case.

Machida et al. (2010) appears to have come to a different conclusion. They found a  $10^2$ -AU scale disk in their 3D nested-grid simulations in the ideal MHD limit (their Model 4), even though their core is strongly magnetized (with a global dimensionless mass-to-flux ratio of  $\lambda = 1$ , see their Table 1). It is unclear whether the disk is rotationally supported or not. If yes, the result would be hard to understand. For such a strongly magnetized core, the mass accumulation at the protostar should produce a strong (split) magnetic monopole in the ideal MHD limit, which is expected to trigger powerful numerical reconnection, as discussed above and shown in Mellon & Li (2008); we have re-run their Model 4 and found the expected episodic reconnections and no rotationally supported disk. There were no reconnections mentioned in their paper, and the apparent lack of reconnection may be an indication that considerable numerical diffusivity acts to reconnect magnetic field lines of opposite polarities efficiently and prevent magnetic flux from accumulating near the protostar to form the expected split monopole in the first place. Since the trapping of magnetic flux at small radii lies at the heart of the efficient braking that renders disk formation difficult in the ideal MHD limit, inability to do so numerically may weaken the braking efficiency artificially and lead to disk formation.

### 6.1.2. *Non-Ideal MHD Effects*

In lightly ionized dense cores of molecular clouds, non-ideal MHD effects are to be expected. Non-ideal effects, particularly ambipolar diffusion and Ohmic dissipation, enable the bulk neutral matter to move across magnetic field lines, breaking the flux freezing condition that is responsible for the formation of the central split magnetic monopole which, in turn, is responsible for the catastrophic disk braking in the ideal MHD limit. The elimination of the central split monopole does not necessarily mean, however, that the magnetic braking would automatically be weakened enough for an RSD to appear. The reason is that the magnetic flux that would be trapped in the central split monopole in the ideal MHD limit is

now concentrated in a small, but finite, circumstellar region instead, as first demonstrated by Li & McKee (1996) in the case of ambipolar diffusion (AD). Krasnopolsky & Königl (2002) showed semi-analytically that the AD-induced flux concentration at small radii can in principle suppress disk formation completely, just as in the ideal MHD limit. Mellon & Li (2009) showed numerically that RSDs are indeed suppressed by a moderately strong magnetic field (with  $\lambda \sim$  several) in the presence of ambipolar diffusion for a reasonable range of cosmic ray ionization rate.

The result of Mellon & Li (2009) is strengthened by the simulations presented in §3.1. We improved over their calculations by self-consistently computing charge densities including dust grains and by extending the computation to the prestellar phase of core evolution leading up to the central mass formation. The extension allows us to explore the angular momentum evolution and disk formation during the transition between the prestellar and protostellar phase of star formation. We find that the tendency to form a disk is stronger around the time of initial protostar formation than at later times (see Fig. 6). This is because there is as yet little magnetic flux accumulated near the center and it takes time for the magnetic braking to remove angular momentum. Once enough magnetic flux has accumulated near the protostar to drive a well-developed accretion (C-)shock, the field strength in the post-shock region is typically strong enough to remove most of the angular momentum of the material falling into the central object, as long as the dense core is moderately strongly magnetized to begin with (with  $\lambda \sim$  a few to several).

The conclusion that the RSD is suppressed by a moderately strong magnetic field in the presence of AD is robust, because the size of the AD shock and the post-shock field strength are rather insensitive to cosmic ray ionization rate and the grain size distribution (see Fig. 7). They are determined mostly by the global requirements that (1) most of the magnetic flux associated with the central stellar mass be redistributed in the post-shock region, and (2) the strong postshock magnetic field be confined by the infall ram pressure (see equations [8] and [10] of Li & McKee 1996), as long as the width of the C-shock is small compared to the radius of the shock. In principle, if the ionization level is decreased by a arbitrarily large factor, the magnetic field would eventually decouple completely from the bulk neutral material and an RSD would form. In practice, however, the RSD is suppressed even for the highly conservative case of both an unrealistically low cosmic ray ionization rate of  $\zeta = 10^{-18} \text{ s}^{-1}$  and an MRN grain size distribution that contains a large amount of small grains (Model LoCR in Table 1). Both the grain growth expected in dense cores and a more realistic (higher) cosmic ray ionization rate tend to make the magnetic field better coupled to the bulk neutral material and the magnetic braking more efficient.

The Ohmic dissipation does not change the above picture much, because the Ohmic

diffusivity  $\eta_O$  is well below the ambipolar diffusivity  $\eta_{AD}$  for the density range  $n_H \lesssim 10^{12} \text{ cm}^{-3}$  that is crucial for disk formation. We can estimate the ratio of the two diffusivities through

$$\frac{\eta_O}{\eta_{AD}} \sim \frac{n_c}{n_e} \frac{1}{\beta_c \beta_e} \quad (6)$$

where the subscripts “ $c$ ” and “ $e$ ” denote, respectively, the charged species whose contribution dominates the AD term and the electrons that are mainly responsible for the Ohmic term. The (dimensionless) Hall parameter  $\beta \equiv \tau\omega$  (where  $\tau$  is the collisional damping time of the motion of a charged species relative to the neutral and  $\omega$  the cyclotron frequency) provides a measure of how well a charge is tied to the magnetic field. The relative unimportance of Ohmic dissipation comes mainly from the fact that electrons are extremely well tied to the magnetic field in the density regime of interest, with  $\beta_e \gg 1$ . For example, at a representative density of  $n_H = 3 \times 10^8 \text{ cm}^{-3}$ , we find  $\beta_e \approx 2 \times 10^5$  for the field strength-density relation given by equation (5). In the large grain (LG) case that we have considered, the AD term is dominated by metal ions,  $M^+$ . Their number density is close to the electron number density ( $n_{M^+} \approx n_e$ ) and they are well tied to the magnetic field at the representative density, with  $\beta_{M^+} \approx 40$ . From equation (6), we expect  $\eta_O/\eta_{AD} \sim 10^{-7}$ , which is in agreement with the computed values shown in the right panel of Fig. 3. In the case of MRN grain size distribution, the AD term is dominated by the small negatively charged grains,  $g^-$ . At the representative density, there are about  $10^2$  small negatively charged grains for each electron ( $n_{g^-} \approx 10^2 n_e$ ) and the small charged grains are marginally tied to the magnetic field  $\beta_{g^-} \sim 1$ . Both the smaller electron abundance and the weaker coupling of the grains to the field tend to make Ohmic dissipation more important relative to ambipolar diffusion. Nevertheless, the electrons are so well tied to the magnetic field that, even in this case, the Ohmic diffusivity is still much smaller than the ambipolar diffusivity, by a factor of  $\sim 2000$  at the representative density. This estimate is again in agreement with the computed values shown in the left panel of Fig. 3.

The Hall effect is expected to be more important than Ohmic dissipation in diffusing the magnetic field in the density regime under consideration. This can be seen from the ratio of Hall and ambipolar diffusivities

$$\frac{\eta_H}{\eta_{AD}} \sim \frac{1}{\beta_c}, \quad (7)$$

which is applicable under the conditions that the same charged species “ $c$ ” dominates both the Hall and AD terms and  $\beta_c \gtrsim 1$ . These conditions are satisfied for the large grain (LG) case at the representative density  $n_H = 3 \times 10^8 \text{ cm}^{-3}$ , where metal ions dominate both terms and  $\beta_{M^+} \approx 40$ . In this case, the Hall diffusivity is only about 2% of the ambipolar diffusivity (but still much larger than the Ohmic diffusivity). It becomes comparable to the ambipolar diffusivity in the case of MRN grain size distribution, where both terms are dominated by

small dust grains that are marginally coupled to the magnetic field (with a Hall parameter  $\beta$  of order unity) at the representative density. At higher densities, the Hall diffusivity is expected to exceed the ambipolar diffusivity as small grains become even less well tied to the magnetic field. However, the contribution from positively charged grains start to cancel out that from negatively charged grains, leaving the Hall diffusivity comparable to the ambipolar diffusivity over a wide range of density (see the left panel of Fig. 3). The Hall effect therefore does not increase the magnetic diffusivity by more than a factor of a few. As such, it is not expected to greatly change the global flow dynamics, especially the structure of the ambipolar diffusion-induced accretion shock, which lies at the heart of the magnetic braking catastrophe. It does, however, introduce a new ingredient into the problem: it can *actively* torque up a magnetized collapsing envelope, even if the envelope is non-rotating to begin with, as first pointed out by Wardle & Ng (1999) and demonstrated numerically in Krasnopolsky et al. (2011; see also C. Braiding 2011). On the scale of several AUs or larger that we can resolve in our non-ideal MHD simulations (§3.4 and 5), the Hall spin-up does not reach the Keplerian speed. The angular momentum gained through Hall spin-up may, however, be conducive to the formation of RSDs on smaller scales, particularly at high enough densities where electrons begin to decouple from the magnetic field and Ohmic dissipation becomes the dominant process for field diffusion (Machida et al. 2010; Dapp & Basu 2010). Nevertheless, the problem of catastrophic magnetic braking that prevents the formation of a sizable RSD of tens of AUs or larger is not resolved through the three non-ideal MHD effects.

## 6.2. Limitations and Future Directions: How to Form RSDs?

We are unable to produce robust, large-scale, rotationally supported disks in our non-ideal MHD simulations for dense cores magnetized to a realistic level. And yet, rotationally supported disks are observed around young stars, at least at relatively late times, after the massive envelope has been removed (which reveals the embedded disk for direct rotation measurement; see Williams & Cieza 2011 for a review). Clearly, one or more assumptions made in our calculations must break down in order for the observed (late-time) RSDs to form. These include (1) assumptions made in the setup of the numerical problem because of computational constraints and (2) additional physical effects that we have not taken into account. We comment on these limitations and their relevance to RSD formation in turn.

### 6.2.1. Numerical Limitations and Possible Ways to Form RSDs

We have restricted our problem setup to 2D (assuming axisymmetry), which greatly reduced the computational demand. A potential drawback is that the imposed symmetry may have enhanced the ability of the AD shock in trapping magnetic flux near the central object, which lies at the heart of the catastrophic magnetic braking that prevents disk formation. The reason is that the high magnetic pressure may force the trapped field lines to escape along the path of least resistance when the axisymmetry is broken. It is plausible that some magnetic flux loaded with relatively little matter (recall that the post-shock region is magnetically subcritical and supported against free-fall collapse by magnetic forces) would act as a “light” fluid and escape in some azimuthal directions, allowing less magnetized fingers of “heavy” material to sink closer to the center in other directions. This type of interchange instability was considered in Li & McKee (1996). It may weaken the magnetic field strength at small radii enough to enable disk formation. Investigation of this possibility is now underway.

Another limitation of the current problem setup is that we adopted a relatively large central hole around the protostar (typically  $10^{14}$  cm or 6.7 AU in radius). We have experimented with smaller holes by a factor of 2–3 in a few cases and found quantitatively similar results. However, it is difficult to reduce the hole size by a much larger factor, because of the constraints on the time step, which decreases as the square of the hole size (assuming the same resolution in the  $\theta$ -direction) in our explicit treatment of the non-ideal MHD terms. A drawback is that we are unable to determine whether small, (sub-)AU-scale RSDs can form during the main protostellar accretion phase or not. The existence of such small RSDs is suggested by the powerful molecular outflows ubiquitously observed around deeply embedded, Class 0 protostars (e.g., Bontemps et al. 1996); they are generally thought to be driven by a fast primary wind launched magnetocentrifugally from the inner part of a Keplerian disk close to the central object (Shu et al. 2000; Königl & Pudritz 2000).

Small RSDs can in principle form at high enough densities where electrons start to decouple from the magnetic field. Before thermal ionization of alkali metals becomes important, the Ohmic dissipation can reduce the local current density, making it hard for the magnetic field to bend in the poloidal plane (which limits the flux accumulation at small radii) and to twist in the azimuthal direction (which weakens magnetic braking; Shu et al. 2006; Machida et al. 2007; Krasnopolsky et al. 2010; Dapp & Basu 2010). A worry is that, in the presence of only ambipolar diffusion and classical Ohmic dissipation, our (2D axisymmetric) calculations showed that little angular momentum is left at the inner edge of the computation domain (6.7 AU), making the formation of RSDs interior to it difficult. However, the Hall effect can spin up the flow that collapses through the inner boundary

to a supersonic (although still locally sub-Keplerian) rotation speed, perhaps making the formation of small RSDs possible. Alternatively, the 3D magnetic interchange instability discussed earlier may weaken the magnetic braking interior to the AD shock enough to facilitate the formation of RSDs in general, and the small RSDs required for fast wind launching in particular. When and how the small RSDs grow to large RSDs observed around relatively evolved YSOs remains uncertain, and may require additional physical effects that have not been investigated in detail in this context to date.

### 6.2.2. *Additional Physical Effects for RSD Formation*

An important ingredient for low-mass star formation is protostellar outflow. It may play a crucial role in disk formation. As first proposed by Mellon & Li (2008; see their §6.2.2), the outflow can strip away the slowly rotating protostellar envelope, which brakes the equatorial infall material that is magnetically linked to it and that tries to spin up and form a rotationally supported disk. Part of the envelope may be removed by the core collapse process itself (see, e.g., Machida et al. 2010) but, if the efficiency of star formation in individual low-mass cores is of order  $1/3$  (Alves et al. 2007; André et al. 2010), the majority of the envelope mass must be removed by some other process, most likely a (fast) protostellar wind (Matzner & McKee 2000). Indeed, the bipolar molecular outflow, thought to be primarily the envelope material swept up by a fast wind (Shu et al. 1991; Shang et al. 2006), is observed to have a narrow jet-like appearance along the axis during the early Class 0 phase and the opening angle at the base increases as the YSO ages (Arce & Sargent 2006). As the fast wind sweeps out an increasingly wider polar region in the envelope, the braking efficiency of the remaining equatorial infall region should decrease, perhaps to a low enough value that a large-scale rotationally supported disk can form.

A specific outflow-enabled large-scale disk formation scenario is as follow. We envision the early formation of a small (perhaps AU-scale) rotationally supported disk (unresolved by the current generation of instruments) during the Class 0 phase, through the processes discussed in §6.2.1. Although the small disk can grow gradually through internal angular momentum redistribution (perhaps gravitational torques rather than magnetic stresses since magnetic decoupling is required for the disk to form in the first place, see discussion in Dapp & Basu 2010), we envision rapid growth in disk size (to, say, 100 AU or more) only during the late phase of envelope removal, when the braking of the equatorial infall material by the envelope is rendered inefficient by outflow stripping. This envelope-depletion induced rapid disk growth may occur towards the end of the main protostellar mass accretion phase, perhaps during the transition from the Class 0 to Class I phases of (low-mass) star formation.



Detailed calculations and high resolution observations, perhaps using ALMA, are needed to test this scenario of late-time formation of a large-scale disk.

Another possibility for large-scale RSD formation is through enhanced magnetic diffusivity. If the diffusivity is greatly enhanced over the classical microscopic values considered in this paper by some processes, the magnetic braking may be weakened enough to allow for RSD formation. Shu et al. (2006) was the first to propose that enhanced Ohmic resistivity may enable RSD formation, and this was demonstrated explicitly in Krasnopolsky et al. (2010). The enhancement in resistivity may come from turbulence (Kowal et al. 2009), which is observed in dense cores from nonthermal line width, or current-driven instabilities (Norman & Heyvaerts 1985), although these effects are hard to quantify at the present time (see, however, Santos-Lima et al. 2010 who have started to quantify the so-called “turbulent reconnection diffusivity”). Similarly, Krasnopolsky et al. (2011) showed that if the Hall diffusivity is large enough, it can enable RSDs to form even in initially non-rotating dense cores.

Numerical diffusion may mimic to some extent enhanced magnetic diffusion of physical origins and lead to large-scale RSD formation. Machida et al. (2010) was able to produce large-scale disks in strongly magnetized cloud cores in both the ideal MHD limit and with a classical (microscopic) value of Ohmic dissipation. However, as we have argued in §6.1.1, the lack of episodic reconnections expected in the ideal MHD limit indicates a considerable numerical diffusion in their calculations. Another indication is that, in the presence of only the classical Ohmic dissipation, we do not find any large-scale RSD (Model REF<sub>O</sub> in Table 1), for a good reason: the Ohmic diffusivity enables the magnetic flux that would have gone into the central object in the ideal MHD limit to accumulate in a small circumstellar region where the magnetic braking is particularly efficient (see Fig. 10), as in the AD case. Such a magnetic flux accumulation was not obvious in Machida et al.’s simulations, which may again indicate an enhanced magnetic diffusion, either of numerical origin or through 3D effects that are not captured by our 2D calculations.

### 6.2.3. *Weak Core Magnetization and RSD Formation*

Here we comment on the possibility that dense star forming cores may be magnetized to different levels, and disks form preferentially in those that are weakly magnetized. Our calculations indicate that, in the presence of ambipolar diffusion, the core mass-to-flux ratio need to be greater than at least  $\sim 10$  in order for a rotationally supported disk to form and survive to late times. Observationally, a mean value of  $\lambda_{los} \approx 4.8 \pm 0.4$  is inferred by Troland & Crutcher (2008) from the line-of-sight field strength for a sample of dark cloud

cores. Applying geometric corrections would reduce the value statistically by a factor of 2–3 (Shu et al. 1999), making it unlikely for the majority of dense cores to be magnetized as weakly as  $\lambda \gtrsim 10$ . Since the majority of, if not all, young stars (formed out of all dense cores) are thought to have an RSD at some point, we consider it unlikely that weak core magnetization is the main reason for RSD formation.

### 6.3. Observational Implications: Disk vs Pseudodisk

We should emphasize that, in our simulations, even though large rotationally supported disks are difficult to form, highly flattened dense “disk-like” structures are prevalent (see Figs. 4, 10, 13, and 15). This is not surprising because, just like rotation, the magnetic field can provide anisotropic support to the cloud core, allowing matter to settle along field lines into flattened structures (Galli & Shu 1993). The fact that there are two types of forces in nature that can retard (anisotropically) the gravitational collapse naturally leads to two types of flattened structures: rotationally supported disks and magnetically induced (pseudo-)disks. If the dense cores are as strongly magnetized as indicated by the currently available observations (with a dimensionless mass-to-flux ratio of several or smaller, see §1), then there is typically more magnetic energy than rotational energy, and a magnetically induced pseudodisk is just as, if not more, likely to form around an accreting protostar as a rotationally supported disk, especially in view of the fact that magnetic braking hinders the formation of rotationally supported disks but not pseudodisks. It is therefore premature to conclude that dense flattened structures observed around deeply embedded protostars (such as from dust continuum observations, e.g., Jørgensen et al. 2009) are rotationally supported disks rather than magnetically induced pseudodisks; the latter can be just as thin as (perhaps even thinner than) rotationally supported disks, because of magnetic compression. To confuse the situation further, the pseudodisks can have a substantial rotation as well (just not enough to provide the full support against gravity) and may or may not collapse at a high speed (see again Figs. 4, 10, 13 and 15). Detailed kinematic information, as well as a knowledge of the central mass, are needed to establish whether a dense flattened circumstellar structure is a rotationally supported disk or not. High resolution observations of the circumstellar magnetic field structure, such as those in Girart et al. (2006), will also go a long way towards testing the idea of magnetically induced pseudodisk (Gonçalves et al. 2008).



## 7. Summary

We have carried out a set of 2D axisymmetric calculations exploring non-ideal MHD effects in magnetic braking and protostellar disk formation in rotating magnetized dense cores. Our main conclusions are summarized as follows:

1. For a realistic magnetic field of moderate strength corresponding to a core mass-to-flux ratio  $\lambda \sim 3\text{--}4$ , the magnetic braking is strong enough to remove essentially all of the angular momentum of the material that accretes onto the central object in the presence of ambipolar diffusion under a wide range of conditions in 2D. Any large-scale (greater than several AUs) rotationally supported disk (RSD) is suppressed by the formation of an ambipolar diffusion-induced accretion shock, which traps a strong magnetic field near the central object, leading to efficient magnetic braking of the post-shock material.

2. On scales greater than  $\sim 10$  AU, realistic levels of Ohmic diffusivity do not enable the formation of large-scale RSDs, either by itself or in combination with ambipolar diffusion. Furthermore, Ohmic dissipation does not necessarily reduce the magnetic braking efficiency. It can make the braking more efficient by enabling magnetic flux accumulation at small radii, where the field strength is increased, similar to the case of ambipolar diffusion.

3. The Hall effect can spin up the post-AD shock material to a significant, supersonic rotation speed, although the rotation remains too sub-Keplerian to form an RSD for the parameter space explored in this work.

4. For an unusually weak magnetic field corresponding to a core mass-to-flux ratio  $\lambda \gtrsim 10$ , a small RSD often forms early in the protostellar accretion phase, when the central mass is still small. In the majority of cases, the RSD disappears at later times, braked strongly by the powerful outflow that it drives. In some cases, particularly when the cosmic ray ionization rate is unusually low and the core rotation rate is unusually high, the fate of the early disk is unknown because the simulation stops early due to numerical difficulty.

5. We discussed several possible ways to enable the formation of large-scale RSDs: magnetic instabilities in 3D, early formation of small RSDs at high densities, outflow stripping of protostellar envelope, enhanced magnetic diffusion and weak core magnetization. The more likely of these possibilities are, in our view, the weakening AD shock in 3D through interchange instability, which is expected to decrease the field strength (and thus the braking efficiency) near the central object, outflow stripping of protostellar envelope, which may allow rapid formation of a large-scale RSD during the transition from the deeply embedded (Class 0) phase to more revealed (Class I and II) phase of low-mass star formation, and enhanced magnetic diffusivity, which may be driven by turbulence-induced reconnections.

This work was supported in part by NASA through NNG06GJ33G and NNX10AH30G, by the Theoretical Institute for Advanced Research in Astrophysics (TIARA) through the CHARMS initiative, and by the National Science Council of Taiwan through grant NSC97-2112-M-001-018-MY3.

## REFERENCES

- Allen, A., Li, Z.-Y., & Shu, F. H. 2003, *ApJ*, 599, 363
- Alves, J., Lombardi, M., & Lada, C. J. 2007, *A&A*, 462, L17
- André, P., et al. 2010, *A&A*, 518, L102
- Arce, H. G., & Sargent, A. I. 2006, *ApJ*, 646, 1070
- Basu, S., & Mouschovias, T. C. 1994, *ApJ*, 432, 720
- Bergin, E. A., & Tafalla, M. 2007, *ARA&A*, 45, 339
- Bodenheimer, P. 1995, *ARA&A*, 33, 199
- Bontemps, S., André, P., Terebey, S., & Cabrit, S. 1996, *A&A*, 311, 858
- Boss, A. P. 1998, *Origins*, 148, 314
- Braiding, C. 2011, unpublished PhD thesis, Macquarie University
- Ciolek, G. E., & Königl, A. 1998, *ApJ*, 504, 257
- Clarke, D. A., Norman, M. L., & Fiedler, R. A. 1994, *ZEUS-3D User Manual* (Tech. Rep. 015; Urbana-Champaign: National Center for Supercomputing Applications)
- Contopoulos, I., Ciolek, G. E., & Königl, A. 1998, *ApJ*, 504, 247
- Crutcher, R. M., Wandelt, B., Heiles, C., Falgarone, E., & Troland, T. H. 2010, *ApJ*, 725, 466
- Dapp, W. B., & Basu, S. 2010, *A&A*, 521, 56
- Dib, S., Kim, J., Vázquez-Semadeni, E., Burkert, A., & Shadmehri, M. 2007, *ApJ*, 661, 262
- Duffin, D. F. & Pudritz, R. E. 2009, *ApJ*, 706, L46
- Fleming, T., P., Stone, J. M. & Hawley, J. F. 2000, *ApJ*, 530, 464

- Galli, D., Lizano, S., Shu, F. H., & Allen, A. 2006, *ApJ*, 647, 374
- Galli, D., & Shu, F. H. 1993, *ApJ*, 417, 243
- Girart, J. M., Rao, R., & Marrone, D. P. 2006, *Science*, 313, 812
- Gonçalves, J., Galli, D., & Girart, J. M. 2008, *A&A*, 490, L39
- Goodman, A. A., Benson, P. J., Fuller, G. A., & Myers, P. C. 1993, *ApJ*, 406, 528
- Heiles, C., & Troland, T. H. 2005, *ApJ*, 624, 773
- Hennebelle, P., & Ciardi, A. 2009, *A&A*, 506, L29
- Hennebelle, P., Commerçon, B., Joos, M., Klessen, R. S., Krumholz, M., Tan, J. C., & Teyssier, R. 2011, *A&A*, 528, A72
- Hennebelle, P., & Fromang, S. 2008, *A&A*, 477, 9
- Hosking, J. G. & Whitworth, A. P. 2004, *MNRAS*, 347, 1001
- Huba, J. D. 2003, in *Space Plasma Simulation*, ed. J. Büchner, C. Dum, & M. Scholer, *Lecture Notes in Physics*, vol. 615 (Berlin: Springer), 166
- Jørgensen, J. K., van Dishoeck, E. F., Visser, R., Bourke, T. L., Wilner, D. J., Lommen, D., Hogerheijde, M. R., & Myers, P. C. 2009, *A&A*, 507, 861
- Königl, A. & Pudritz, R. 2000, in *Protostars and Planets IV*, eds. V. Mannings et al. (Univ. of Arizona Press), 759
- Königl, A., Salmeron, R. & Wardle, M. 2010, *MNRAS*, 401, 479
- Kowal, G., Lazarian, A., Vishniac, E. T., & Otmianowska-Mazur, K. 2009, *ApJ*, 700, 63
- Kudoh, T., & Basu, S. 2011, *ApJ*, 728, 123
- Kunz, M. W., & Mouschovias, T. C. 2010, *MNRAS*, 408, 322
- Krasnopolsky, R., Königl, A. 2002, *ApJ*, 580, 987
- Krasnopolsky, R., Li, Z.-Y. & Shang, H. 2010, *ApJ*, 716, 1541
- Krasnopolsky, R., Li, Z.-Y. & Shang, H. 2011, *ApJ*, in press
- Li, Z.-Y., & McKee, C. F. 1996, *ApJ*, 464, 373

- Lizano, S., & Shu, F. H. 1989, *ApJ*, 342, 834
- Mac Low, M.-M., Norman, M. L., Königl, A., & Wardle, M. 1995, *ApJ*, 442, 726
- Machida, M. N., Inutsuka, S., & Matsumoto, T. 2007, *ApJ*, 670, 1198
- Machida, M. N., Inutsuka, S., & Matsumoto, T. 2010, arXiv:1009.2140
- Masunaga, H., & Inutsuka, S. 2000, *ApJ*, 531, 350
- Matzner, C. D. & McKee, C. F. 2000, *ApJ*, 545, 364
- Mathis, J. S., Ruml, W., & Nordsieck, K. H. 1977, *ApJ*, 217, 425
- Mellon, R. R., & Li, Z.-Y. 2008, *ApJ*, 681, 1356
- Mellon, R. R., & Li, Z.-Y. 2009, *ApJ*, 698, 922
- Nakamura, F., & Li, Z.-Y. 2005, *ApJ*, 631, 411
- Nakano, T., & Nakamura, T. 1978, *PASJ*, 30, 671
- Nakano, T., Nishi, R., & Umebayashi, T. 2002, *ApJ*, 573, 199
- Nishi, R., Nakano, T., & Umebayashi, T. 1991, *ApJ*, 368, 181
- Norman, C. A., & Heyvaerts, J. 1985, *ApJ*, 147, 247
- Pagani, L., Steinacker, J., Bacmann, A., Stutz, A., & Henning, T. 2010, *Science*, 329, 1622
- Padovani, M., Galli, D. & Glassgold, A. E. 2009, *A&A*, 501, 619
- Price, D. J., & Bate, M. R. 2007, *Ap&SS*, 311, 75
- Sano, T., & Stone, J. M. 2002, *ApJ*, 570, 314
- Santos-Lima, R., Lazarian, A., de Gouveia Dal Pino, E. M., & Cho, J. 2010, *ApJ*, 714, 442
- Shang, H., Allen, A., Li, Z.-Y., Liu, C.-F., Chou, M.-Y., & Anderson, J. 2006, *ApJ*, 649, 845
- Shu, F. H., Allen, A., Shang, H., Ostriker, E. C. & Li, Z.-Y. 1999, in *The Origins of Stars and Planetary Systems*, eds. C. J. Lada & N. D. Kylafis (Kluwer), 193
- Shu, F. H., Galli, D., Lizano, S., & Cai, M. 2006, *ApJ*, 647, 382
- Shu, F. H. & Li, Z.-Y. 1997, *ApJ*, 475, 251

- Shu, F. H., Najita, J. Shang, H. & Li, Z.-Y. 2000, in *Protostars and Planets IV*, eds. V. Mannings et al. (Univ. of Arizona Press), 789
- Shu, F. H., Ruden, S. P., Lada, C. J. & Lizano, S. 1991, *ApJ*, 370, 31
- Tafalla, M., Mardones, D., Myers, P. C., Caselli, P., Bachiller, R., & Benson, P. J. 1998, *ApJ*, 504, 900
- Tassis, K., & Mouschovias, T. C. 2007, *ApJ*, 660, 388
- Tilley, D. A., & Pudritz, R. E. 2005, *Protostars and Planets V*, 8473
- Troland, T. H., & Crutcher, R. M. 2008, *ApJ*, 680, 457
- Ward-Thompson, D., Kirk, J. M., Crutcher, R. M., Greaves, J. S., Holland, W. S., & André, P. 2000, *ApJ*, 537, L135
- Ward-Thompson, D., Motte, F., & André, P. 1999, *MNRAS*, 305, 143
- Wardle, M., & Königl, A. 1993, *ApJ*, 410, 218
- Wardle, M., & Ng, C. 1999, *MNRAS*, 303, 239
- Webber, W. R. 1998, *ApJ*, 506, 329
- Williams, J. P., & Cieza, L. A. 2011, *ARA&A*, in press